Direct numerical simulations of turbulent pipe flow laden with finite-size neutrally buoyant particles at low flow Reynolds number

Cheng Peng & Lian-Ping Wang

Acta Mechanica

ISSN 0001-5970
Volume 230
Number 2

Acta Mech (2019) 230:517-539
DOI 10.1007/s00707-018-2268-2

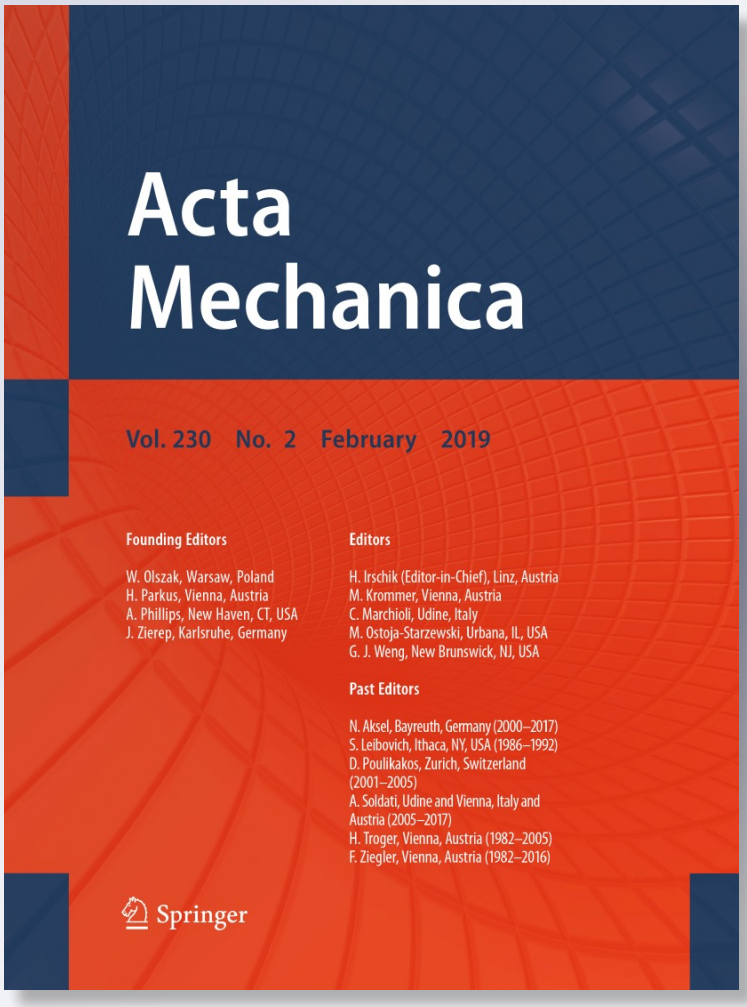

Springer

Acta Mech 230, 517–539 (2019)
https://doi.org/10.1007/s00707-018-2268-2

ORIGINAL PAPER

Cheng Peng · Lian-Ping Wang

Direct numerical simulations of turbulent pipe flow laden with finite-size neutrally buoyant particles at low flow Reynolds number

Received: 29 March 2018 / Revised: 30 June 2018 / Published online: 24 October 2018

Abstract In this paper, turbulent pipe flows laden with finite-size particles are investigated, using the direct numerical simulations based on the lattice Boltzmann method. Our focus is on the modulation of turbulence statistics in the pipe due to the presence of finite-size neutrally buoyant particles, and the question if the characteristics of modulation differ from those in a turbulent channel flow under comparable system parameters in order to reveal the effect of curved walls in the pipe. The mechanisms responsible for modulations of the turbulent intensity in the pipe flow are clarified through a quantitative budget analysis of the turbulent kinetic energy.

1 Introduction

Mutual interactions between the suspended particles or droplets and the carrier fluid turbulence in a turbulent particle-laden flow represent a fundamental topic in multiphase flow, and the characteristics and consequences of such interactions are of great importance to many applications in engineering and natural processes. However, the current understanding of turbulence modulation by dispersed particles remains very limited and incomplete [1]. Previous experimental and numerical investigations revealed that there exist several competing mechanisms for dispersed particles to augment or suppress fluid turbulence. It seems unreasonable to expect a simple formulation for the net effect, given the many controlling parameters of particle-laden flow systems.

Systematic investigation of turbulence modulation by particles can be traced back to 1980s. Gore and Crowe summarized the earlier experimental observations on jet and pipe flows, and they concluded that particles with diameters d_p greater than about 10% of the integral length scale l_e tend to augment turbulence, while smaller particles have an opposite effect [2,3]. Here $l_\mathrm{e} \equiv u'^3/\epsilon$, u' is the root-mean-square fluctuation velocity, ϵ is the viscous dissipation rate. Kulick et al. [4] conducted experiments in a fully developed turbulent flow in a vertical channel with glass and copper beads smaller than the Kolmogorov scale and found that turbulence is attenuated, with the level of attenuation increasing with increasing particle Stokes number St ($St = \tau_\mathrm{p}/\tau_K$, where τ_p is the particle response time $\tau_\mathrm{p} = \rho_\mathrm{p} d_\mathrm{p}^2/(18\rho_\mathrm{f}\nu)$, ρ_p, ρ_f are the particle and fluid

C. Peng (✉) · L.-P. Wang
Department of Mechanical Engineering, University of Delaware, Newark, DE 19716-3140, USA
E-mail: cpengxpp@udel.edu
Tel.: +1-302-831-0831
Fax: +1-302-831-3619

L.-P. Wang
Department of Mechanics and Aerospace Engineering, Southern University of Science and Technology, Shenzhen, China
E-mail: wanglp@sustc.edu.cn; lwang@udel.edu
Tel.: +86-0755-8801-8169; +1-302-831-8160
Fax: +1-302-831-3619

density, respectively, ν is the fluid kinematic viscosity, and τ_K is the Kolmogorov time scale $(\nu/\epsilon)^{(1/2)}$) and mass loading. Paris later extended Kulick et al.'s work by bringing the particle Reynolds number into the investigation [5]. Here the particle Reynolds number was defined as $Re_p = d_\mathrm{p} U_\mathrm{T}/\nu$, where U_T is the terminal settling velocity of the particle in a quiescent fluid. Particles with larger Re_p were reported to result in more significant attenuation of turbulence. Kussin and Sommerfeld measured the modulations of turbulent intensity in a fully developed turbulent flow in a horizontal channel [6]. While the turbulent attenuation induced by particles with sizes smaller than Kolmogorov scale was again confirmed, the maximum attenuation was observed in the streamwise direction, in contrast to the transverse direction reported by Kulick et al. This difference is likely resulted from the different experimental settings on the direction in which the gravity is aligned, relative to the mean flow direction. Kussin and Sommerfeld also studied the effect of wall roughness on turbulence modulation by particles [6]. Larger wall roughness was found to result in stronger attenuation on turbulence. This observation indicates that the turbulence modulation not only depends on the properties of the dispersed phase, but the carrier turbulent flow as well. In light of these later observations, Tanaka and Eaton [7] proposed a new non-dimensional parameter, particle momentum number Pa, to qualify the sign of turbulent modulations with a more comprehensive consideration of the roles played by the particle Stokes number St, particle size and the flow Reynolds number. Tanaka and Eaton compiled 80 sample points from earlier experimental measurements and concluded that turbulence augmentation happened with either very large Pa ($Pa > 10^5$) or very small Pa ($Pa < 10^3$), where $Pa = StRe_L^2 \left(\frac{\eta}{L}\right)^3$, $Re_L = UL/\nu$ is the characteristic flow Reynolds number, L and U are the characteristic length and the velocity of the flow, respectively, while turbulence attenuation occurred for $10^3 < Pa < 10^5$. Although this analysis provides empirical guidance for engineering practices, it is still hard to make physical connections between Pa and the mechanisms responsible for modulation of turbulent kinetic energy. It is also vague why the dependence of turbulence modulation on Pa is not monotonic. Later, Bellani et al. [8] experimentally investigated the effects of particle shapes on the turbulence modulation in a homogeneous isotropic turbulence. They found that spherical particles attenuated the turbulent intensity five times larger than the attenuation brought by ellipsoidal particles, suggesting that turbulence modulation is more complex and deserves further investigation.

At the current stage, the knowledge gap in turbulence modulation mainly concerns the size of the dispersed particles. When the size is comparable or larger than the Kolmogorov length of the carrier turbulent flow, the discontinuity and distortion induced by the dispersed phase at the fluid–solid interfaces must be fully considered, implying that the disturbed flow around each particle should be adequately resolved in a turbulent particle-laden flow [9]. Although conducting sub-Kolmogorov scale measurements inside the boundary layers around particles is possible (although still difficult) [10], experimental investigations still suffer from difficulties to extract full data to form a complete picture of turbulence modulation. So far, experiments serve more in providing global or average turbulence statistics to be used as benchmark results for numerical simulations. On the contrary, numerical simulations, particularly the direct numerical simulations (DNS), provide essentially every detail in a particle-fluid two-phase system, thus being a powerful tool for the investigation of various turbulence modulation mechanisms. The key aspect in the numerical simulation is to apply the no-slip condition on each particle surface, a necessary condition for achieving reliable conclusions on the turbulence modulation [11].

DNS capable of resolving the no-slip condition on the particle surfaces are referred as the interface-resolved DNS (IRDNS), a tool that has been rapidly developed in recent years, for decaying homogeneous isotropic turbulent flows [12,13], forced homogeneous isotropic turbulent flows [14,15], and turbulent channel flows [16,17] laden with many finite-size particles. In IRDNS, multiple numerical methods are used to simulate the fluid turbulence and to treat the fluid–solid interfaces, as discussed in a recent review by Maxey [18]. Based on the mesh type used in the simulations, the methods of IRDNS can be roughly classified into two categories. The first category uses body-fit meshes that are attached to particle surfaces, including the arbitrary Lagrangian-Eulerian method [19] and the overset mesh simulations[20,21]. Though considered to be highly accurate, these methods are constrained by their massive computational cost in the mesh regeneration process; thus, they have only been applied to systems with a relatively few particles. For systems involving a large number of moving particles, the second category of methods based on fixed Eulerian grids is much more efficient computationally. Prosperetti and his colleagues developed PHYSALIS, a sharp interface treatment, which is a hybrid method combining the analytic solutions of Stokes flows near the particle surfaces and the

regular N-S solver elsewhere [22,23]. The basic idea of PHYSALIS is to expand the flow in a thin shell around the particle based on the Stokes flow solution and match the coefficients of the expanding series with the numerical solutions coming from outside. PHYSALIS has been applied in [24] for a homogeneous isotropic turbulence passing a single static particle and an array of static particles, and in [22] for a weakly decaying homogeneous isotropic turbulence laden with 100 solid particles. The immersed boundary methods (IBM) are so far the most popular method being used for IRDNS [17,25]. IBM converts the representation of the actual particle surfaces into an external force applied to the surrounding fluid nodes that enforces the no-slip constraint [26,27]. A regularized-δ function is used to interpolate the velocity on the particle surface from the grid point and the local boundary-induced body force back to the fluid nodes. Extra Lagrangian grids are typically attached to each particle for better representation of particle surfaces. Another method sharing the idea of converting the no-slip boundary as a body force is known as the fictitious domain (FD) methods, where the body force is applied in the region occupied by particles to enforce rigid-body rotation [28,29]. The applications of FD methods have been realized in a few IRDNS such as particle-laden turbulent channel flow [16] and turbulent pipe flow [30].

Besides the above studies where conventional methods are used to solve the N-S equations, the lattice Boltzmann method (LBM) also contributed to a few IRDNS in the recent years, e.g., in homogeneous isotropic turbulence [13,14,31], and turbulent channel flows [32,33]. LBM solves mesoscopic gas kinetic equation whose moments can be made to be equivalent to the macroscopic N-S equations in the incompressible limit [34, 35]. At the level of the Boltzmann equation, the no-slip condition can be realized either mesoscopically or macroscopically. For example, the incorporation of IBM into LBM led to IRDNS of particle-laden flows in a forced homogeneous isotropic turbulence [14], and a fully developed channel turbulence [33]. Alternatively, the non-slip condition in LBM can also be directly realized through local interpolated bounce-back schemes [36, 37]. IRDNS in turbulent flows based on the latter can be found in our previous studies [13,31,32]. Treating the fluid–solid interfaces by IBM may be viewed as a smoothed interface method, and by interpolated bounce-back then a sharp interface method which tends to be more accurate while prone to numerical instability.

In this study, we extend our previous studies of IRDNS in a turbulent channel flow to a turbulent pipe flow. The former flow has been simulated a few times previously [16,17,32,33], but IRDNS of the latter flow has only been reported once in [30]. When particles are absent, a significant distinction exists between the mean velocity profiles of the two flows, while the log-law is well established in the turbulent channel flow with a relatively low Reynolds number, the same profile is not observed in the turbulent pipe flow even with a much higher flow Reynolds number [38–40]. This is related to the wall curvature in the latter case, and the effect of this difference on the nature of turbulence modulation has not been elucidated. By contrasting the simulation results of particle-laden turbulent channel flows to those in particle-laden turbulent pipe flows, the current study is aimed at addressing this specific aspect. Another objective of the present study is to analyze the turbulence modulation mechanisms in the particle-laden turbulent pipe flow. This analysis will shed insight into the earlier experimental observations [2].

The rest of the paper is outlined as follows. In Sect. 2, the physical problem investigated in the present work and the simulation set-up are summarized. The lattice Boltzmann method, with implementation details on handling the no-slip fixed and moving boundaries and short-range particle–particle and particle–wall interaction forces are provided. In Sect. 3, the flow statistics obtained from the current simulations are presented, and compared with those generated in particle-laden turbulent channel flows with comparable settings. A budget analysis of the modified turbulent kinetic energy in the particle-laden turbulent pipe flow is also provided to identify the physical mechanisms responsible for turbulence modifications. Finally, a summary is provided in Sect. 4.

2 Problem statement and the simulation method

2.1 Statement of the physical problem and resolution requirement

We consider the classical turbulent flows in a circular pipe. As shown in Fig. 1, the carrier flow in a circular pipe with a radius R and a length L is driven by a constant body force g (per unit mass). r, θ and z represent the radial, azimuthal and streamwise coordinates, respectively. At the fully developed (or statistically stationary) state, and since spherical solid particles can only make a point contact, the balance between the total driving force and the viscous wall drag is established as $2\pi RL\langle\tau_w\rangle = \pi R^2 L\rho_f g$, which leads to the expression of the averaged wall shear stress $\langle\tau_w\rangle$ and the friction velocity u_τ as

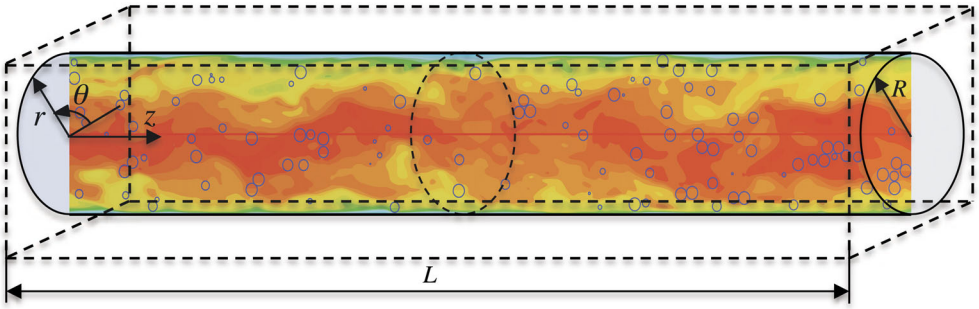

Fig. 1 Diagrams of a particle-laden pipe flow simulation

Table 1 Key physical parameters used in the simulations. Parameters from the second to the last column are: computational domain size, pipe radius (half channel width), friction velocity, friction Reynolds number, grid resolution, particle size, particle amount, total particle volume fraction, particle/fluid density ratio

Case #	$N_x \times N_y \times N_z$	R	L/R	Re_τ	$\delta x/y_\tau$	d_p^+	N_p	Φ_p	$\rho_\mathrm{p}/\rho_\mathrm{f}$
p0	$300 \times 300 \times 1799$	148.5	12.11	180	1.212	(–)	(–)	(–)	(–)
p1	$300 \times 300 \times 1799$	148.5	12.11	180	1.212	29.09	861	5%	1.0
p2	$300 \times 300 \times 1799$	148.5	12.11	180	1.212	14.54	6887	5%	1.0
Case #	$N_x \times N_y \times N_z$	H	L/H	Re_τ	$\delta x/y_\tau$	d_p^+	N_p	Φ_p	$\rho_\mathrm{p}/\rho_\mathrm{f}$
c0	$1800 \times 299 \times 600$	149.5	12.04	180	1.204	(–)	(–)	(–)	(–)
c1	$1800 \times 299 \times 600$	149.5	12.04	180	1.204	28.90	2231	5%	1.0
c2	$1800 \times 299 \times 600$	149.5	12.04	180	1.204	14.45	17845	5%	1.0

$$\langle \tau_w \rangle = \frac{1}{2}\rho_\mathrm{f} g R, \quad u_\tau = \sqrt{\frac{\langle \tau_w \rangle}{\rho_\mathrm{f}}} = \sqrt{\frac{gR}{2}}. \tag{1}$$

The friction Reynolds number $Re_\tau = u_\tau R/\nu$ is fixed at 180. The inlet and outlet of the pipe are assumed to be periodic. The no-slip boundary condition is applied to the pipe wall and particle surfaces. In this paper, we examine one single-phase flow case (Case p0) and two particle-laden flow cases (Case p1 and Case p2) with different particle sizes. In all three cases, we keep the driving force g and viscosity ν identical. There are several considerations when defining the domain size. First, the grid resolution in the radial direction needs to be sufficient to resolve all the length scales in the flow. For $Re_\tau = 180$, published DNS datasets in a turbulent channel flow [41,42] have revealed that the local Kolmogorov scale near wall is about $\eta^+ \approx 1.5$, where superscript $+$ in the present study always means normalized by wall unit $y_\tau \equiv \nu/u_\tau$. To resolve this smallest length scale, we choose $R = 148.5\delta_x$, where δ_x is the spatial spacing of a lattice grid which corresponds to $\delta_x^+ = 1.212$. Second, the pipe length should be long enough in order to eliminate the effects of periodicity in the streamwise direction. Here, for all three cases, we choose $L \approx 12.11R$, which, according to the study of Ref. [43], is sufficient to retain length-independent turbulent statistics in most flow regimes. At last, particles should occupy enough grid spacings such that the boundary layers around particles are resolved. The boundary layer thickness around a particle roughly obeys $\delta \sim d_\mathrm{p}/\sqrt{Re_\mathrm{p}}$ [44], where d_p is the particle diameter and $Re_\mathrm{p} = \|\Delta\mathbf{u}\| d_\mathrm{p}/\nu$ is the particle Reynolds number defined based on the mean flow velocity difference $\|\Delta\mathbf{u}\|$ between solid and fluid phases. In our simulation, since the particles move freely with the bulk stream, Re_p is typically small except near the pipe wall. Thus, for the two particle-laden cases, we choose $d_\mathrm{p} = 12\delta_x, 24\delta_x > \sqrt{Re_\mathrm{p}}\delta_x$, respectively. Combining all these considerations, the key parameters in the three cases are summarized in Table 1.

In order to assess the effects of the curved pipe wall on the flow modulation due to the presence of particles, three corresponding turbulent channel flow cases, i.e., one single-phase (Case c0) and two particle-laden flow cases (Case c1 and c2) with different particle sizes are also simulated to serve as baselines to assess the results obtained in the turbulent pipe flow simulations. For fair comparisons, the parameters in the three channel flow cases are chosen to be comparable to their counterparts in three pipe flow cases, as shown in Table. 1. In particular, the spanwise length of the channel is chosen as $L_z = 4H$, where $H = 149.5\delta_x$ is the half channel width. This setting allows the channel flow to have comparable spanwise distance as in the pipe flow, in terms

of area-weighted average spanwise length, namely, $L_{\text{span}} = \frac{1}{\pi R^2}\int_0^R (2\pi r) \times (2\pi r \mathrm{d}r) = 4\pi R/3 \approx 4R$. At stationary, the driving force and viscous drag are balanced as $2\rho_{\text{f}} g H L_x L_z = 2L_x L_z \langle \tau_w \rangle$. Again, we fix the driving force g in the three channel flow cases.

2.2 The lattice Boltzmann method

The lattice Boltzmann method (LBM) is used for our fluid flow simulation. A typical LBM is based on a cubic grid system in a Cartesian coordinate system. To obtain a better isotropy for the flow in a cylindrical coordinate system [45,46] and a better numerical stability [47], we choose LBM based on the D3Q27 lattice grid. In contrast to the conventional computational fluid dynamics (CFD) methods, LBM solves the evolution of mesoscopic particle distribution functions as

$$\mathbf{f}\left(\mathbf{x} + \mathbf{e}_i \delta_t, t + \delta_t\right) - \mathbf{f}\left(\mathbf{x}, t\right) = -\mathbf{M}^{-1}\mathbf{S}\left[\mathbf{m}\left(\mathbf{x}, t\right) - \mathbf{m}^{(\text{eq})}\left(\mathbf{x}, t\right)\right] + \mathbf{M}^{-1}\Psi, \tag{2}$$

where $\mathbf{f}$ is the distribution function vector, t and $\mathbf{x}$ are the time and spatial location, respectively. $\mathbf{e}_i$ is the lattice velocity in ith direction. For a D3Q27 lattice grid, there are 27 lattice velocities labeled from 0 to 26. δ_t is the time step size. The right-hand side (RHS) of Eq. (2) is known as collision operator. Here we choose the multi-relaxation-time (MRT) model due to its greater flexibility and better numerical stability [47–49]. The collision in the MRT model is handled in the moment space (or hydrodynamic space). For the D3Q27 lattice, we define a moment vector $\mathbf{m}$ with 27 independent elements based on a linear transformation of the distribution functions as $\mathbf{m} = \mathbf{M}\mathbf{f}$, $\mathbf{f} = \mathbf{M}^{-1}\mathbf{m}$, where $\mathbf{M}$ is a 27×27 transformation matrix, and $\mathbf{m}^{(\text{eq})}$ being the equilibrium moments vector. $\mathbf{S}$ is a diagonal matrix contains relaxation parameters, whose entries can be optimized to enhance the numerical stability. The last term on the RHS, $\mathbf{M}^{-1}\Psi$ represents the effect of external body force in LBM, where Ψ is the mesoscopic forcing vector in the moment space, which is discussed in detail in [47]. Typically, LBM based on the standard collision-propagation algorithm has second-order accuracy in velocity and first-order accuracy in pressure [50]. Compared with the second-order finite-difference discretization of the Navier–Stokes equations, LBM usually has better accuracy since the propagation of distribution function is exact and it introduces no artificial diffusion to the simulation [51].

2.3 The treatment of no-slip boundary condition in LBM

The no-slip boundary condition on a solid surface in LBM can be treated in two alternative manners. The first is the immersed boundary method (IBM) that converts a no-slip boundary to a distribution of local body force [52,53]. In the past, many particle-laden flow simulations based on LBM were reported with this type of treatments [14,33]. On the other hand, in LBM, the second method to realize the no-slip boundary condition is the bounce-back scheme, which is more intrinsic to the zero lattice particle momentum relative to the surface [36,54–56]. In the bounce-back schemes, the unknown distribution functions at the boundary nodes are directly constructed such that the no-slip velocity constraint at those node points is satisfied. Since the number of unknown distribution functions is usually larger than that of hydrodynamic constraints, the bounce-back schemes are usually not unique. On straight and static surfaces, for example, on the channel walls, the mid-link bounce-back [36] can be naturally applied with the conversed second-order accuracy. On the other hand, interpolation bounce-back schemes are required to ensure a second-order or higher accuracy on curved surfaces [54,55]. Unlike the immersed boundary method that involves a local regularization, *i.e.*, local interpolation of velocity and pseudo-body force between Lagrangian and Euler grids, the bounce-back schemes that are being processed linkwise introduce less numerical diffusion to the system, thus lead to more accurate results [57,58]. However, due to the lack of numerical diffusion, LBM simulations incorporating the bounce-back scheme is prone to numerical instability.

In the simulations presented in this paper, the no-slip boundary condition on the curved pipe surface and the particle surfaces are handled by the linear interpolated bounce-back scheme in [55] and the quadratic interpolated bounce-back scheme in [54], respectively. The principle to choose those schemes is to first satisfy the numerical stability, then to strive for a higher accuracy. In the past, the robustness of those two schemes were validated in a single-phase turbulent pipe flow simulation [47], and a number of particle-laden turbulent flow simulations [13,31,32]. However, to maintain desired second-order accuracy, both schemes require at least two grid points on the fluid side to proceed the interpolation. In the scenario where the number of grid points

is not sufficient to implement the above interpolation, e.g., when two solid bodies are too close to each other, the amendment is to use the single-node second-order bounce-back scheme recently proposed by [56]. This scheme only uses the distribution functions on the boundary node itself, but still preserves the second-order accuracy in boundary treatment.

When the bounce-back schemes are adopted for the no-slip boundary treatment, the most natural way to evaluate the hydrodynamic forces and torques acting on the particles is the momentum exchange method (MEM), which obtains the hydrodynamic forces and torques by summing up the momentum/moment exchange between the solid and fluid phases in each time step [36,59,60]. To ensure Galilean invariance in the hydrodynamic force evaluation, the Galilean invariance momentum exchange method (GIMEM) proposed in [60] is adopted. This scheme was validated in a number of particulate flow simulations [61,62]. Unlike the fictitious domain methods (e.g., immersed boundary methods, immersed body methods) where the whole computational domain is filled with fluid [18], in the present simulations the volume occupied by the particles is excluded from the flow evolution and there is no fluid information on the corresponding grid nodes. When a particle moves to a new location, the information must be initialized on the nodes uncovered by the particle. This process is known as refilling. Considering the numerical efficiency, the refilling scheme proposed in [63] is adopted. Further details about the schemes for boundary treatment, hydrodynamic force evaluation and refilling process can be found in the original literature cited above.

2.4 Particle–particle and particle–wall interaction

In the simulations, when two particles are very close or in physical contact, the interaction force between the two particles are no longer resolved. The same statement applies to the situation involving a particle and the pipe wall. Models representing the short-range hydrodynamic interaction, a.k.a., the lubrication force, and the collision detection algorithms should be included to restore the correct interaction forces in these situations. For the short-range hydrodynamic interaction, we choose the lubrication force correction in [64], which reads

$$\mathbf{F}_{ij}^{\mathrm{lub}} = -6\pi\mu_{\mathrm{f}} r_{\mathrm{p}} \mathbf{u}_n \left[\lambda(\epsilon) - \lambda(\epsilon_0)\right], \tag{3}$$

where $\mathbf{F}_{ij}^{\mathrm{lub}}$ is the lubrication force between the ith particle and the jth particle. μ_{f} is the dynamic viscosity of the fluid, $\mathbf{u}_n$ is the longitudinal relative velocity between the centers of the two particles, r_{p} is the particle radius, and λ is a function of normalized gap distance $\epsilon = \delta / r_{\mathrm{p}}$. ϵ_0 is the threshold distance below which the lubrication correction is turned on. For particle–particle interaction, λ is defined as

$$\lambda(\epsilon) = \frac{1}{2\epsilon} - \frac{9}{20}\ln\epsilon - \frac{3}{56}\epsilon\ln\epsilon + 1.346, \tag{4}$$

while for particle–wall interaction, we use

$$\lambda(\epsilon) = \frac{1}{\epsilon} - \frac{1}{5}\ln\epsilon - \frac{1}{21}\epsilon\ln\epsilon + 0.848. \tag{5}$$

In our particle-laden turbulent pipe flow simulations, the threshold distances ϵ_0 for particle–particle and particle–wall interaction are set to 0.125 and 0.15, respectively. Note that although Eq. (5) is derived for the interaction between a spherical particle and a flat wall, it is still adopted for particle-curved pipe wall collision in the present simulations since the curvature of the pipe wall is much smaller than the particles. In order to avoid the singularity when ϵ approaches to 0, Eq. (3) is applied piecewisely as suggested in [64]. The physical contact collision between two solid objects are handled with the soft-sphere collision (SSC) model developed in [64]. Such model simplifies the interaction between two colliding objects as a spring-dashpot force, which reads

$$\mathbf{F}_{ij}^{ssc} = \left(-k_n\delta - \beta_n u_n\right)\mathbf{n}_{ij}, \tag{6}$$

where

$$k_n = \frac{m_e\left[\pi^2 + (\ln e_d)^2\right]}{(N_{\mathrm{c}}\delta_t)^2}, \qquad \beta_n = -\frac{2m_e(\ln e_d)}{N_{\mathrm{c}}\delta_t}, \tag{7}$$

are the stiffness of the spring and the damping coefficient of the dashpot. e_d is the dry collision coefficient of restitution. In our simulation, the collisions are assumed nearly elastic, thus e_d is set as 0.97. $N_{\mathrm{c}}\delta_t$ is the collision period (δ_t is the time step size). Physically, N_{c} should be set as small as possible since contact collisions happen

almost instantaneously. However, N_c is suggested to be no less than 8 to fully resolve a collision process [64]. We have tested different values of N_c in both particle–particle and particle–wall dry collisions. In general, a larger N_c results in actual coefficients of restitution closer to the targeted value but represents a softer spring that may lead to unphysical overlapping between two solid objects. We set $N_c = 12$ in our simulations. To better resolve the collision process, a refined particle integration time step size $\mathrm{d}t = 0.1\delta_t$ is applied to update the particle motion with the neighboring fluid flow unchanged within δt.

After the forces and torques (including both resolved hydrodynamic forces and the modeled particle–particle (wall) interaction forces) are obtained, the translational velocity $\mathbf{V}$, positions $\mathbf{Y}$, angular velocity $\boldsymbol{\Omega}$ and displacement $\boldsymbol{\Theta}$ of the ith particle are updated as

$$\mathbf{V}_i^{t+\mathrm{d}t} = \mathbf{V}_i^t + \frac{1}{M_\mathrm{p}}\left[\frac{\mathbf{F}_i^{t+\delta_t/2} + \mathbf{F}_i^{t-\delta_t/2}}{2} + \sum_j \left(\mathbf{F}_{ij}^{\mathrm{lub}} + \mathbf{F}_{ij}^{ssc}\right)^t\right]\mathrm{d}t, \tag{8a}$$

$$\mathbf{Y}_i^{t+\mathrm{d}t} = \mathbf{Y}^t + \frac{1}{2}\left(\mathbf{V}_i^t + \mathbf{V}_i^{t+\mathrm{d}t}\right)\mathrm{d}t, \tag{8b}$$

$$\boldsymbol{\Omega}_i^{t+\mathrm{d}t} = \boldsymbol{\Omega}_i^t + \frac{1}{I_\mathrm{p}}\left[\frac{\mathbf{T}_i^{t+\delta_t/2} + \mathbf{T}_i^{t-\delta_t/2}}{2}\right]\mathrm{d}t, \tag{8c}$$

$$\boldsymbol{\Theta}_i^{t+\mathrm{d}t} = \boldsymbol{\Theta}^t + \frac{1}{2}\left(\boldsymbol{\Omega}_i^t + \boldsymbol{\Omega}_i^{t+\mathrm{d}t}\right)\mathrm{d}t, \tag{8d}$$

with distinct particle time step size $\mathrm{d}t$ and fluid time step size δ_t.

2.5 Validation: single-phase turbulent channel and pipe flows

We have performed a series of validation tests for the numerical method and its implementation details, which can be found in [65]. For the sake of conciseness, we briefly show the comparisons of some turbulence statistics between our LBM simulations with the established databases for the single-phase turbulent channel (Case c0) and pipe (Case p0) flows. The statistics of mean velocity profiles, Reynolds stress profiles and the root-mean square (r.m.s.) velocity profiles of different components are shown in Figs. 2, 3, and 4, respectively. These statistics are averaged over the two homogeneous directions, *i.e.*, the streamwise and the azimuthal (spanwise) directions, and also over different time frames covering 30 to 50 large eddy turnover times, after the flow reaches the stationary state. Therefore, they are presented as functions of only the wall-normal locations. For the turbulent channel flow, the results from the pseudo-spectral simulation of Kim et al. [41] are used as references, while for the turbulent pipe flow, the benchmark results are extracted from the spectral simulations of Loulou et al. [39], Chin et al. [43], and El Khoury et al. [66] as well as the finite-difference simulation of Wagner et al. [67]. In all cases, our results match well the simulation data from other methods.

3 Results and discussion

In this section, we focus on analyzing the turbulent statistics for both fluid and particulate phases. By default, the average is restricted to a specific phase, i.e., the volume occupied by the other phase is excluded in obtaining the statistics,

$$\begin{aligned}\text{in a channel: } \langle Q\rangle &= \frac{1}{\Delta T}\int_t^{t+\Delta T}\frac{\int_0^{L_x}\int_0^{L_z} Q\chi\,\mathrm{d}x\mathrm{d}z}{\int_0^{L_x}\int_0^{L_z}\chi\,\mathrm{d}x\mathrm{d}z}\mathrm{d}t,\\ \text{in a pipe: } \langle Q\rangle &= \frac{1}{\Delta T}\int_t^{t+\Delta T}\frac{\int_0^{L_z}\int_0^{2\pi} Q\chi r\,\mathrm{d}z\mathrm{d}\theta}{\int_0^{L_z}\int_0^{2\pi}\chi r\,\mathrm{d}z\mathrm{d}\theta}\mathrm{d}t,\end{aligned} \tag{9}$$

where Q is any quantity of concern, χ is the phase indicator, which is equal to 1 in the respective phase (fluid or solid) and 0 in the other phase (solid or phase). Since the LBM simulations are conducted on a Cartesian grid, the results must be transferred to cylindrical coordinates first before averaging. The binning strategy used in the present simulations is similar to the one introduced in [47]. However, to better quantify the results near the

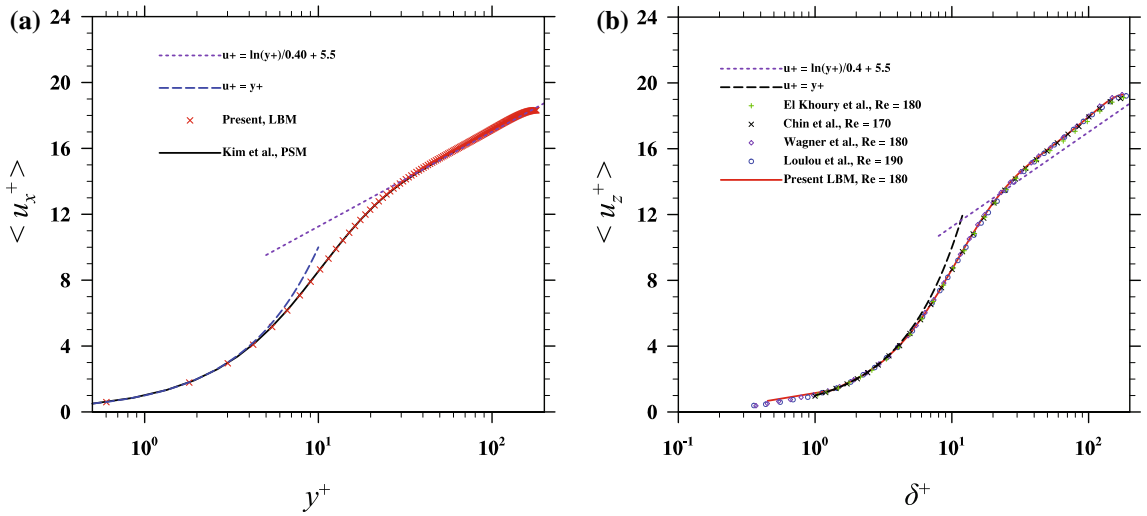

Fig. 2 Mean velocity profiles of: **a** a single-phase turbulent channel flow, **b** a single-phase turbulent pipe flow

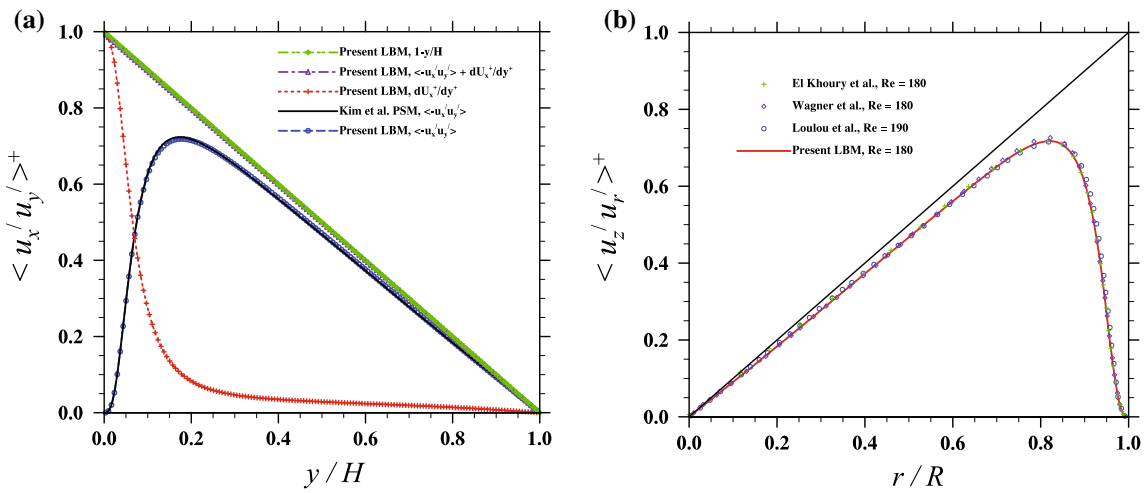

Fig. 3 Reynolds stress profiles of: **a** a single-phase turbulent channel flow, **b** a single-phase turbulent pipe flow

pipe wall, a finer bin size with a width of $\mathrm{d}r^+ = 0.9$ is applied to the region $\delta^+ = (R - r)^+ \leq 36$, compared to a coarse bin size $\mathrm{d}r^+ = 1.8$ otherwise. This setting leads to a total number of 120 bins, i.e., 40 fine bins near the pipe wall and 80 coarse bins farther away.

The bulk flow velocity over the whole domain

$$U_b = \frac{1}{\Delta T} \int_t^{t+\Delta T} \left(\frac{\int\int\int_V u \chi \mathrm{d}V}{\int\int\int_V \chi \mathrm{d}V} \right) \mathrm{d}\tau, \tag{10}$$

where χ is 1 in the fluid volume and 0 in solid volume, in each simulation is compiled in Table. 2. The presence of particles reduces the overall flow speed in all particle-laden cases. In both channel and pipe flows, large particles result in larger flow velocity reduction than small particles. Particles in a turbulent pipe flow modify the flow speed more than their counterparts in a turbulent channel flow. With the same particle volume fraction (5%), the bulk flow velocity in a turbulent pipe flow is reduced by 8.2% and 6.7% by large and small particles, respectively. In a turbulent channel flow, the corresponding values are 6.1% and 2.8%.

As shown by the negative slopes in the profiles of mean velocity difference (Fig. 5c), the reduction of the bulk flow velocity in the presence of particles is mainly due to the smaller velocity gradients in the particle-laden flows within the buffer region ($8 \leq y^+(\delta^+) \leq 30$). While the velocity of the fluid phase increases rapidly with the increasing distance from the wall in the buffer region, the velocity of the particulate phase increases

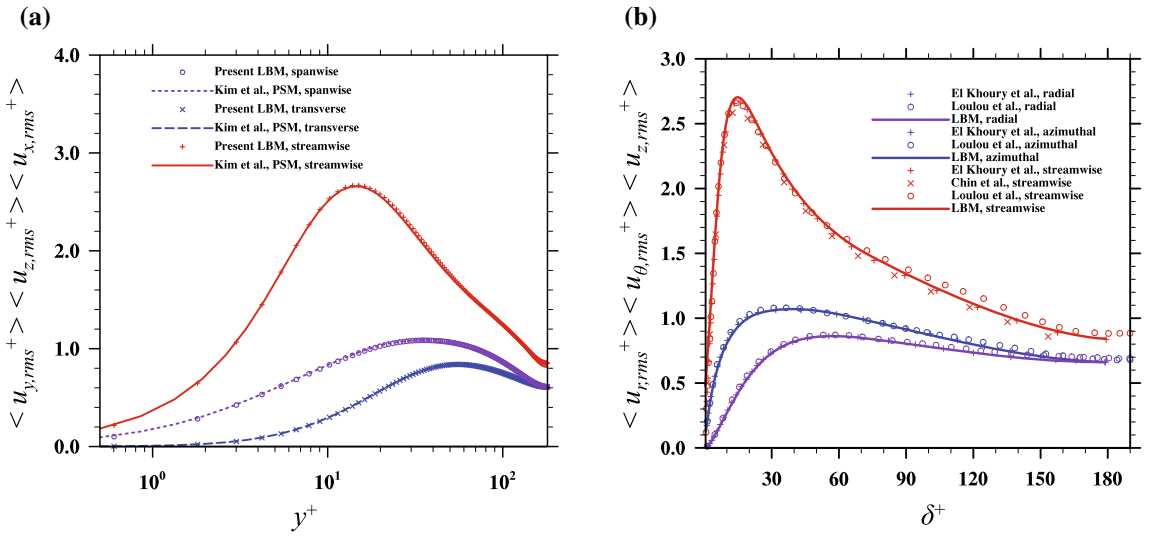

Fig. 4 R.m.s. velocity profiles of: **a** a single-phase turbulent channel flow, **b** a single-phase turbulent pipe flow

Table 2 The bulk flow speed in turbulent channel and pipe flows

Case #	c0	Kim et al. [41]	c1	c2	p0	Loulou et al. [39]	p1	p2
U_b^+	15.73	15.63	14.77	15.28	14.74	14.77	13.56	13.78

less rapidly, as shown in Fig. 6. This is because in the volume occupied by particles, the mean velocity gradient is twice of the mean angular velocity of the particle rotation, which is small due to the spatial correlation inside a particle. Due to the no-slip constraint, the fluid in the ambient region of particles also tend to have smaller local average velocity gradient, which impact the rate of change of fluid velocity. Due to the curvature of the circular pipe, the relative volume taken by the buffer region in a pipe is larger than that in a plane channel flow. Therefore, the overall velocity reduction in the pipe flow is relatively more significant. Compared to small particles, large particles spread their negative impact on the mean velocity gradient over a large range of wall-normal locations. As indicated by the ranges of negative slopes in Fig. 5c, which extend to $y^+(\delta^+) \approx 30$ in the large-particle cases but end at $y^+(\delta^+) \approx 20$ in the small-particle cases. Therefore, the bulk flow velocity is reduced more in the large particle cases than the corresponding small particle cases.

Since particles can have slip motion on the channel and pipe walls (Fig. 5d), the near wall fluid are expected to be accelerated by the particle motion. However, the only significant acceleration occurs in the small particle case in a turbulent channel flow. Although large particles have greater slip velocity than small particles (Fig. 5d), the acceleration is more obvious when small particles are present. This is probably because large-particle cases have a smaller local volume fraction (Fig. 10), and an even smaller local particle surface area than the small-article cases in the near wall region to accelerate the flow there. For the same particle size and volume fraction, the accelerations in a turbulent pipe flow are smaller than those in a turbulent channel flow, even though the slip velocities of particles are comparable in the flows (Fig. 5d). This difference contributes partially to the smaller flow speed reduction in the former.

When particles are present, the slopes of the mean velocity profiles in the log-law region become larger than the unladen cases. This observation was also reported in [17,33] in particle-laden turbulent channel flow simulations. The mean velocity profiles in the range of $40 \leq y^+(\delta^+) \leq 140$ in each particle-laden case can still be described by logarithmic functions with modified coefficients as presented in Fig. 7. Interestingly, the two cases in a turbulent channel flow have very similar slopes, so do the two cases in the turbulent pipe flow. The particle size seems to have no significant impact on the slope of velocity profile in the logarithmic region. Picano et al. [17] and Eshghinejadfard et al. [33] conducted particle-laden turbulent channel flow simulations with varying particle volume fractions, their results suggested the particle volume fraction had a more evident effect on the slopes, that a larger mean particle volume fraction leads to a larger slope.

An interesting question to ask is that, whether the mean velocity profiles shown in Fig. 7 can be fitted to a universal log-law under certain rescaling. Luchini argues that a universal log-law exists between the single-

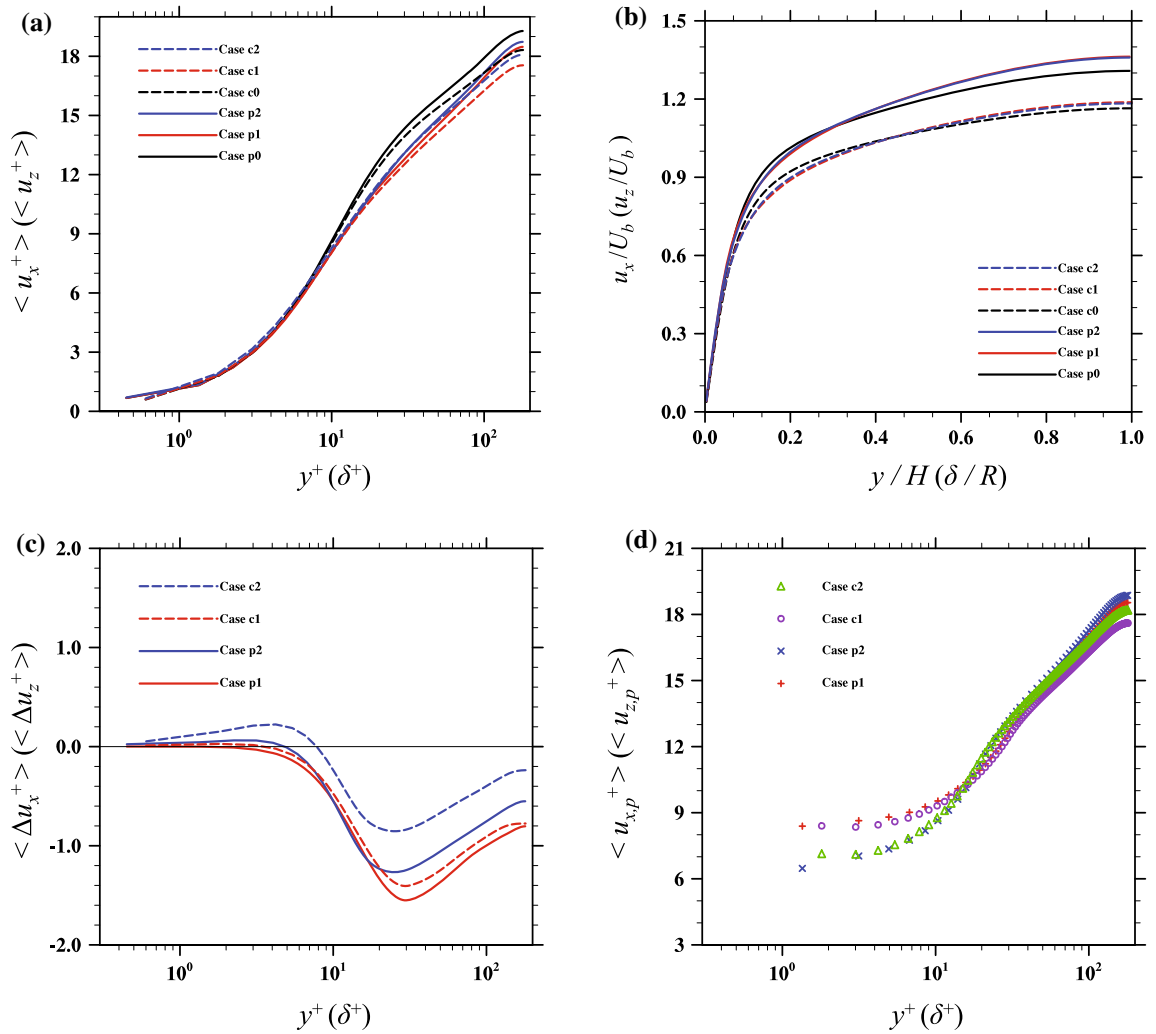

Fig. 5 Profiles of **a** the mean fluid velocity, normalized by the wall unit, **b** the mean fluid velocity, normalized by the bulk flow velocity, **c** the mean fluid velocity difference relative to the respective single-phase flow case, **d** the mean particle velocity. Note that z is the streamwise direction in the pipe flow cases, while x is the streamwise direction in the channel flow cases

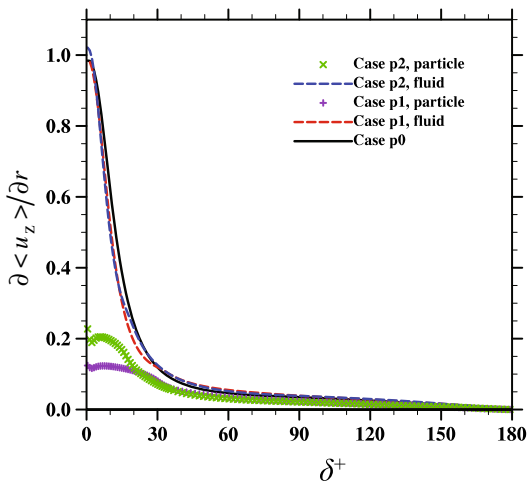

Fig. 6 Profiles of mean velocity gradients in the single-phase and particle-laden pipe flow simulations

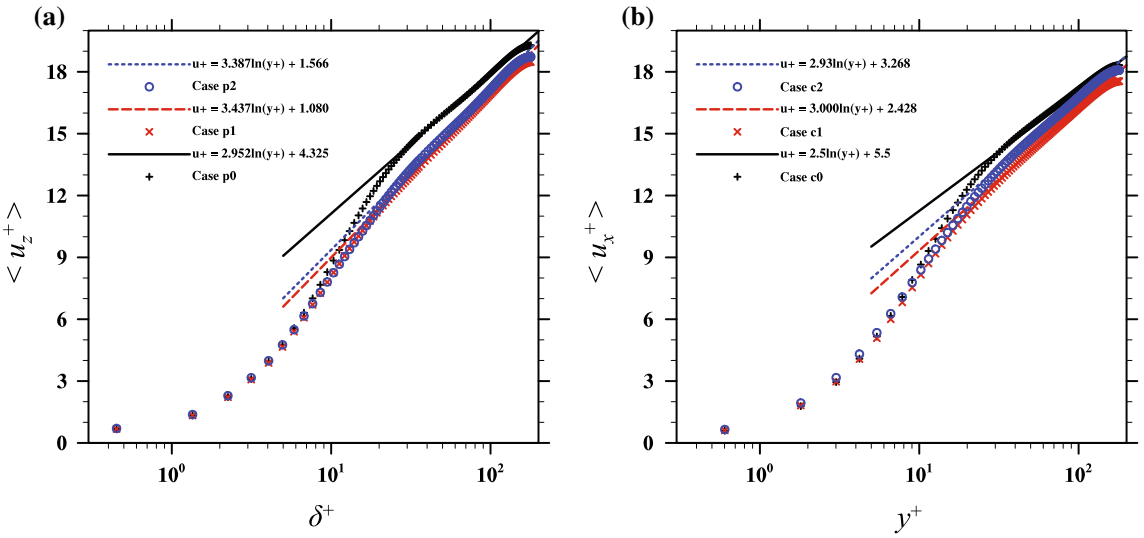

Fig. 7 Mean velocity profiles fitted with modified log-laws: **a** pipe flow cases, **b** channel flow cases

phase channel and pipe flows as the geometry effect can be absorbed as a linear correction term of the driving pressure gradient [68]. The driving pressure gradient is not an independent parameter of the wall shear stress according to the global force balance, thus it did not appear in the previous derivation of the log-law. However, inside the logarithmic region, the driving pressure gradient and the wall shear stress are somehow separated. This is because locally the fluid does not strongly feel the wall stress, as the logarithmic region is far away from the wall, but it is still driven by the same mean pressure gradient. The log-law proposed by Luchini can be written as

$$u^+ = \frac{1}{\kappa}\ln y^+ + \frac{\gamma G}{Re_\tau} y^+ + B, \tag{11}$$

where $G = -H\rho_f g/\langle\tau_w\rangle$ is the geometry parameter, which takes $G = 1$ in a plane channel and $G = 2$ in a circular pipe flow. By fitting in the DNS datasets of $Re_\tau = 1000$, Luchini reported Eq. (11) with $\kappa = 0.392$, $\gamma = 1$ and $B = 4.48$ was able to describe the mean velocity profiles of plane channel, circular pipe and turbulent boundary layer flows at the same time. To examine whether this theory can be extended to particle-laden flows, we use the mean velocity data in our pipe flow simulations to obtain the values of κ, γ and B, and then examine whether the velocity profiles of the corresponding channel flow simulations can fit in. The data points within the range of $40 \le u^+ \le 100$ are used. For the single-phase, large-particle, and small-particle cases, our DNS data yield $(\kappa, \gamma, B) = (0.420, 0.666, 6.199)$, $(0.330, 0.532, 2.394)$, $(0.354, 0.659, 3.423)$. The velocity profiles of the six simulations subtracting each's second term in Eq. (11) are shown in Fig. 8. While the corresponding velocity profiles of the channel and pipe flow do show certain levels of similarity under Luchini's log-law, obvious differences are still observed. This might be because the Reynolds number in the present simulations is too small for the inner and outer regions of a wall-bounded turbulent flow to separate. In fact, as shown in [68], the universal log-law starts to be valid at $y^+ \approx 200$, which is already larger than the normalized half channel width or pipe radius in the present simulations. For small Re_τ, contributions from higher-order expansions in $1/Re_\tau$ may be significant, making the universal log-law less applicable. Another practical issue to contrast our simulation results against Eq. (11) is the limited data points in the logarithmic-law range used to determine the values of κ, γ, and B. In our simulations, since the Re_τ is low, the range of the wall-normal locations within the logarithmic-law range is narrow. This makes the values of the κ, γ, and B sensitive to the data points used for curve fitting.

Another effort to formulate a universal log-law was made by Costa et al. [69]. Unlike the effort of Luchini trying to unify the log-law in different single-phase wall-bounded turbulent flows, Costa et al. tried to propose a log-law that is applicable for both single-phase and particle-laden turbulent channel flow. Costa et al.'s idea comes from the observation that particles have a local high concentration near the wall. When the particle volume fraction is high enough, such local concentration may lead to a particle layer that separate the direct interactions between the flow on its two sides. For the flow outside (closer to the channel center than the particle layer), the particle layer acts as a virtual wall. Costa et al. argue that the log-law in the single-phase turbulent

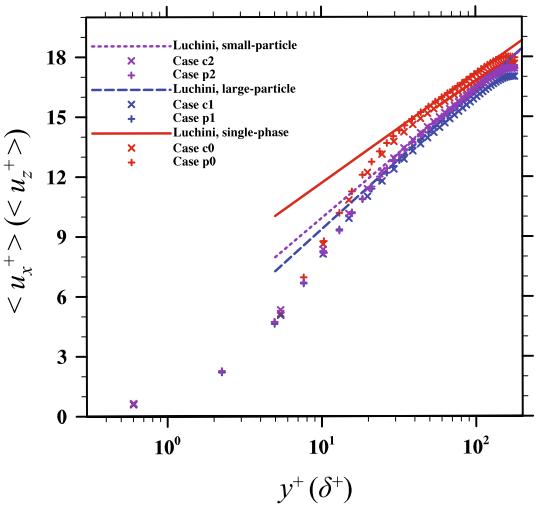

Fig. 8 Profiles of mean velocity fitted to the universal log-law of Luchini [68]

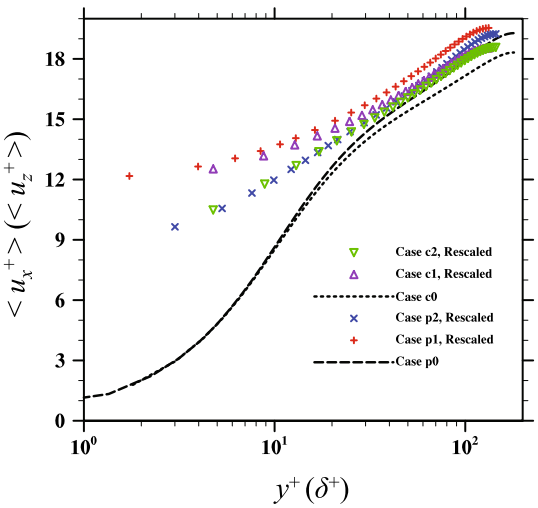

Fig. 9 Profiles of mean velocity fitted to the universal log-law of Costa et al. [69]

channel flow may be able to apply to this outer region with a redefined effective viscosity results from the particle suspension. In summary, the universal log-law proposed by Costa et al. can be written as

$$\frac{\langle u \rangle}{u_\tau^*} = \frac{1}{\kappa} \ln \frac{y - \delta_{pw}}{y_\tau^*}, \tag{12}$$

where $u_\tau^* = u_\tau \sqrt{(H - \delta_{pw})/H}$ is the effective friction velocity in the particle-laden flows, κ is the von Karman constant in single-phase turbulent channel flow. $\delta_{pw} = 1.5 d_\mathrm{p} \left(\phi_\mathrm{p}/0.6\right)^{1/3}$ is the location of the virtual wall, $y_\tau^* = \nu^e / u_\tau^*$ is the effective wall unit calculated by the effective viscosity $\nu^e = (1 + (5/4)\phi_\mathrm{p}/(1 - \phi_\mathrm{p}/0.6))^2 \nu$ in the homogeneous suspension region. The mean velocity profiles in our particle-laden simulations rescaled by Eq. (12) are shown in Fig. 9. Under this rescaling, the slopes $(1/\kappa)$ of the profiles in the log-law region in the particle-laden cases do become closer to the slopes in their corresponding single-phase cases, but the values of constant B are different from once case to another. In Costa et al.'s theory, the constant B remains the same in both single-phase and particle-laden flows. This difference is probably because the particle volume fraction in our simulations is not large enough (although Costa et al. did include the simulation of Picano et al. [17] with a same particle volume fraction 5% in their study to validate their theory). The log-law of Costa et al. is based on the assumption that particles are able to form a layer that separates the flow into distinct two parts. Whether this assumption is applicable in our simulations is questionable. Although particles do have

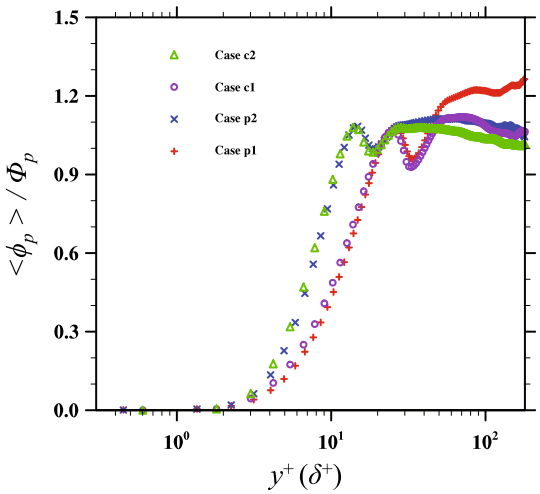

Fig. 10 Profiles of particle volume fraction in the particle-laden turbulent channel and pipe flows

a local concentration near the wall (see Fig. 10), this concentration does not lead to a local particle volume fraction significantly higher than the bulk particle volume fraction (it is also true in Costa et al.'s simulations), thus whether the particles will form a layer is not certain. Intuitively, with the same particle volume fraction, the smaller size particles have a large possibility to form a particle layer due to their larger total surface area than the larger size particles. This effect of particle size is not considered in Eq. (12). In Eq. (12), only δ_{pw} depends on the particle size, but δ_{pw} only measures the location of the particle layer, not the possibility of the formation of the particle layer.

Finally, when normalized by the bulk flow velocity in each case (see Fig. 2b), we observe a quite similar effect induced by particles on the mean velocity profiles. Compared to their counterparts in the unladen cases, the mean velocity profiles in the particle-laden cases become more convex, with smaller values in the buffer region and larger values near the channel center.

The profiles of particle volume fraction normalized by the field-mean volume fraction in each case are presented in Fig. 10. Near the wall, the distribution of particles in a turbulent channel flow is almost identical to that in a turbulent pipe flow with the same particle size. The volume fractions of large particles are smaller than those of small particles because the no-penetrating wall restricts the appearance of the former more than the latter in the near wall region. In each case, the particle volume fraction increases from zero at the wall till it reaches a local maximum point. As analyzed in [65], this local maximum point corresponding to the wall-normal location where the wall-induced repulsive force due to the lubrication effect [70] pointing toward the channel/pipe center balances with the shear-induced and rotation-induced lift forces [71], both pointing toward the wall due to the larger translational velocity of the particulate phase than its fluid counterpart. Farther away from the wall, the particle volume fraction decreases and reaches a local minimum point. This minimum point likely results from the change of direction of shear-induced and rotation-induced lift forces since the mean velocity of the fluid phase eventually catches up with the mean velocity of the particulate phase. The major difference of the particle volume fractions in the two flows occurs near the center of channel/pipe. In a turbulent channel flow, the particle volume fractions near the channel center are almost uniform with small descending slopes. Such descending slopes are due to the weak lift forces pointing toward the wall, which has been well recognized as the "Segré-Silberberg effect" [71,72]. In a turbulent pipe flow, the decreasing particle volume fraction resulting from the lift force is compensated by the shrinking pipe volume near the pipe center. In the case of turbulent pipe flow laden with large particles, the particle volume fraction near the pipe center even increases with the distance from the pipe wall, as a single large particle in this region occupies a significant part of the total volume.

The Reynolds stress profiles in the simulations are shown in Fig. 11. The presence of particles can either increase or decrease the Reynolds stress, depending on the particle size and type of the background flow. In general, small particles result in more Reynolds stress enhancement than large particles in the same flow, and the same size particles generate more Reynolds stress enhancement in a channel flow than in a pipe flow, as indicated by Fig. 11b. Particles in a turbulent channel or pipe flow can have two opposite effects on the Reynolds stress. On the one hand, due to their finite-sizes, particles follow the fluctuation motion

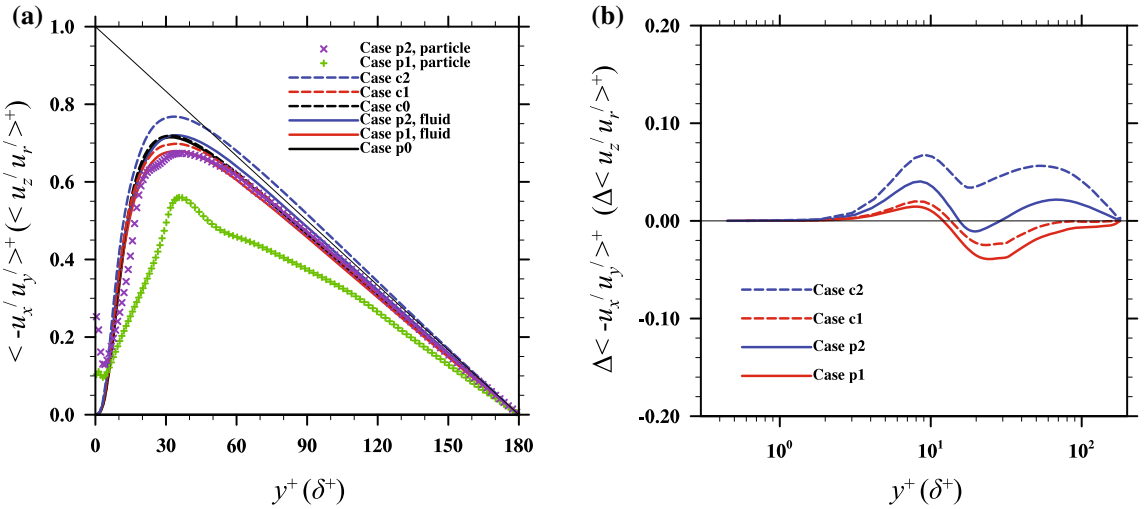

Fig. 11 Profiles of: **a** Reynolds stress, **b** relative change of Reynolds stress from the single-phase flows

less than the fluid and serve as dampers to the turbulent motion. The larger the particle size is, the more significant spatial filtering particles can provide to the turbulent intensity. On the other hand, in a turbulent channel (or pipe) flow, the statistics of $u_x' u_y'$ (or $u_z' u_r'$) are dominated by the ejection and sweeping events. The particle rotation, especially the rotation in the spanwise (or azimuthal) direction, induces additional ejection and sweeping events that further increase the value of $u_x' u_y'$ (or $u_z' u_r'$). Since small particles can have a larger magnitude of particle angular velocity as well as a larger total surface area, they are more likely to result in a more significant enhancement of Reynolds stress than large particles. The evidence of this rotation-induced enhancement can be found in [65], where we simulated the particle-laden turbulent channel flow with freely rotating and no-rotating finite-size particles. When all parameters being identical, the restriction of particle rotation resulted in a significant reduction of the Reynolds stress when compared to the freely rotating particle cases. Particles in the near wall regions experience the strongest lift forces and as such can develop more jumpy translational motions, which contributes to the local Reynolds number enhancement. This effect is indicated by the larger Reynolds stress in particular phase than its fluid counterpart for $\delta^+ \leq 5$ (Fig 11a). The resulting modulation on the Reynolds stress depends on the relative strength of the above two competing mechanisms. For small particles in a turbulent channel flow, the rotation-induced enhancement is always larger than the spatial-filtering-induced attenuation so the Reynolds stress is enhanced everywhere. In the other three cases, the enhancement mechanism overwhelms the attenuation mechanism near the wall where the particles rotate most rapidly and bear the strongest lift forces, while reduced in the buffer region where the filtering effect is maximized as the Reynolds stress due to the wall reaches a peak. Farther away from the wall, the enhancements due to the particle rotation of large particles become insufficient to compensate the damping effect due to the particle filtering, so the two large-particle cases lead to reduction of Reynolds stress. In the case of small particles in a turbulent pipe flow, the opposite is observed.

The profiles of turbulent kinetic energy (TKE) $\langle k^+ \rangle = \langle 0.5 u_i' u_i' \rangle$ are presented in Fig. 12. The presence of particles generally results in a more homogeneous distribution of TKE along the wall-normal direction in both turbulent channel and pipe flows, with enhanced TKE near the wall and significantly reduced TKE in the buffer region. Close to the channel and pipe centers, TKE is augmented by the small particles but attenuated by the large particles. Similar to the modulation of Reynolds stress, small particles in each flow always result in a higher TKE than large particles probably because their smaller size makes them damp the turbulent fluctuations less than large particles. While TKE in the single-phase turbulent channel and pipe flows are almost identical except near the wall, TKE in the turbulent channel flow is larger than that in turbulent pipe flow at the same particle size at most wall-normal locations. The profiles of component-wise TKE are presented in Figs. 13, 14, and 15 for the streamwise, wall-normal and spanwise (azimuthal) velocity components in terms of r.m.s. velocities. The modulations induced by particles on the streamwise r.m.s. velocity in each case are similar to the total TKE; reductions in the buffer region and enhancements in the near wall region and the channel center region can be observed. Particles in a turbulent channel flow still lead to larger streamwise r.m.s. velocity than particles in a turbulent pipe flow in the region $y^+ (\delta^+ \leq 30)$, but the opposite is observed in the

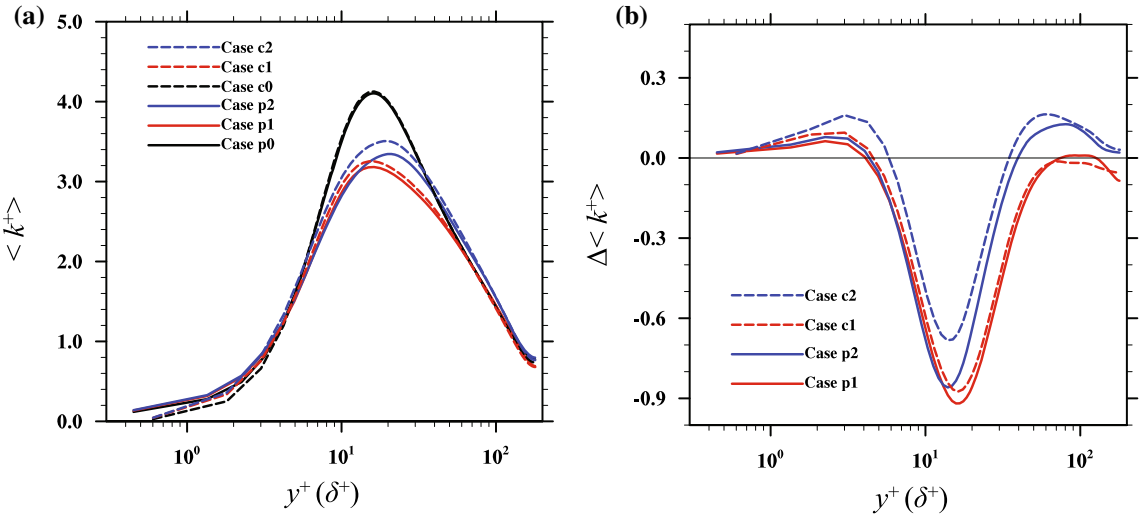

Fig. 12 Profiles of: **a** turbulent kinetic energy, **b** relative change of turbulent kinetic energy from the single-phase flows

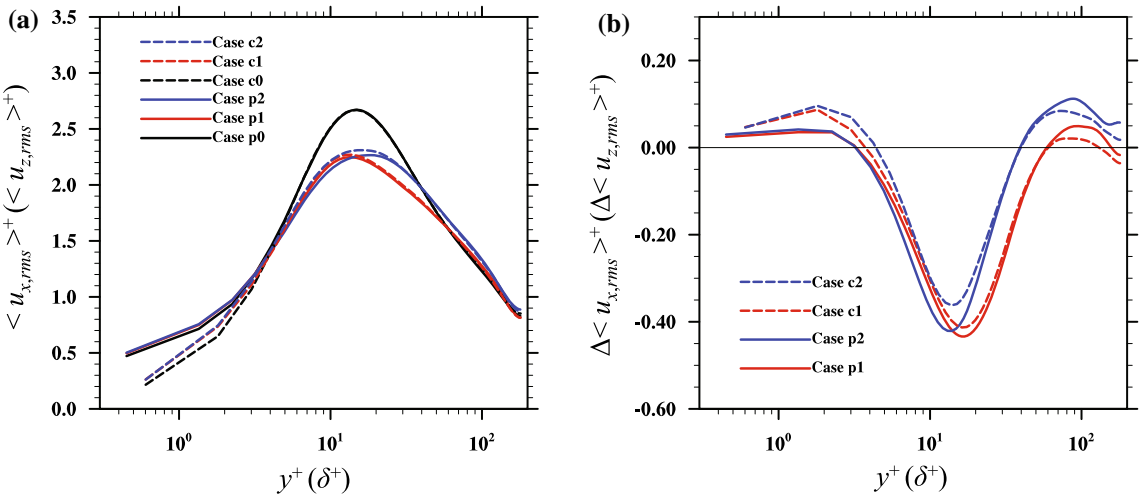

Fig. 13 Profiles of: **a** streamwise r.m.s. velocity, **b** relative change of streamwise r.m.s. velocity from the single-phase flows

channel or pipe center region. The wall-normal and spanwise (azimuthal) r.m.s. velocities in the particle-laden flows are significantly greater than those in the single-phase flows at $y^+(\delta^+ \leq 30)$. Again, in most of the regions particles in a turbulent channel flow result in larger wall-normal and spanwise r.m.s. velocities than their counterparts in a turbulent pipe flow. Since the modulations by the particles likely originate from the particle surfaces, the fact that the particles with the same volume fraction induce a larger relative surface area in a turbulent channel flow than a turbulent pipe flow may be responsible. In a turbulent channel flow, the ratio between the particle surface area and the area of the channel walls is $N_\mathrm{p} 4\pi R_\mathrm{p}^2/(2L_x L_z)$, which translates into $3H\Phi_\mathrm{p}/R_\mathrm{p}$. In a turbulent pipe flow, on the other hand, the ratio becomes $N_\mathrm{p} 4\pi R_\mathrm{p}^2/(2\pi RL) = 3R\Phi_\mathrm{p}/(2R_\mathrm{p})$. Since the two flows have comparable H and R, the relative increase in solid surface in the turbulent channel flow is twice as large as that in the turbulent pipe flow, which may bring a larger overall impact. Other than the relative magnitudes, we find that the flow modulations induced by particles are qualitatively similar in the turbulent channel and pipe flows. The curvature of the pipe only brings about a quantitative impact on the level of modulation.

To help understanding the modulation induced by particles in the turbulent pipe flow, the budget equation of the turbulent kinetic energy is derived. The detailed derivation can be found in the appendix of [65] through the theory of volume averaging [73], which is not repeated here. In a particle-laden turbulent pipe flow, if the control volume V is chosen as a cylindrical ring of finite bin width stretching over the streamwise direction,

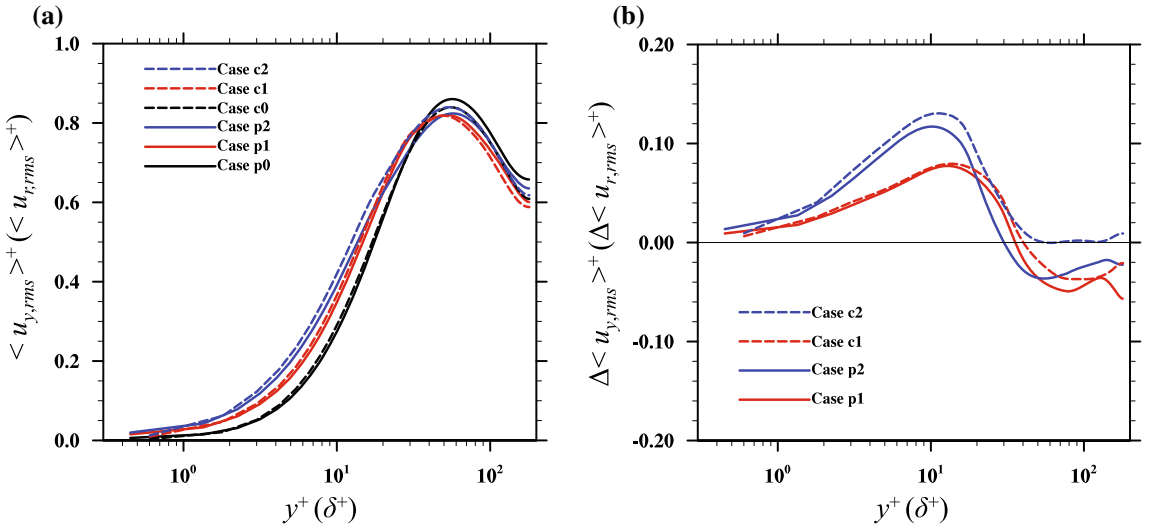

Fig. 14 Profiles of: **a** radial r.m.s. velocity, **b** relative change of radial r.m.s. velocity from the single-phase flows

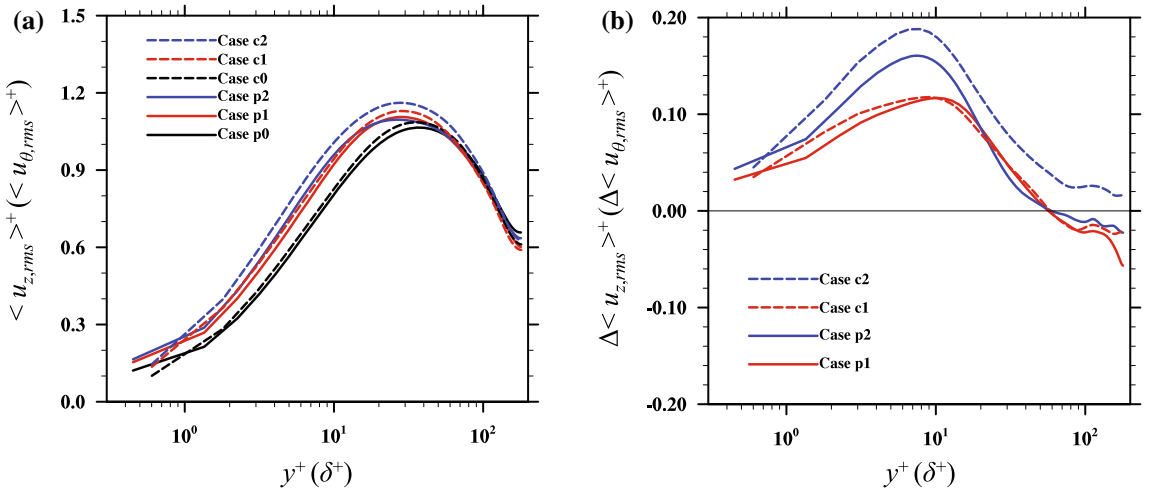

Fig. 15 Profiles of: **a** azimuthal r.m.s. velocity, **b** relative change of azimuthal r.m.s. velocity from the single-phase flows

i.e., statistics are averaged over the streamwise and azimuthal directions, the budget equation of fluid TKE reads

$$\begin{aligned}\frac{\partial}{\partial t}\alpha\frac{1}{2}\langle u_i'u_i'\rangle = &\underbrace{-\alpha\langle u_z'u_r'\rangle\frac{\partial\langle u_z\rangle}{\partial r}}_{E_{\mathrm{P}}}\underbrace{-\frac{1}{r}\frac{\partial}{\partial r}r\alpha\frac{1}{2}\langle u_i'u_i'u_r'\rangle}_{E_{\mathrm{TT}}}\underbrace{-\frac{1}{\rho}\frac{\partial}{\partial r}\alpha\langle p'u_r'\rangle}_{E_{\mathrm{PT}}}\underbrace{+\frac{1}{\rho r}\frac{\partial}{\partial r}r\alpha\langle\tau_{ir}'u_i'\rangle}_{E_{\mathrm{VT}}}\\ &\underbrace{-\frac{\alpha}{\rho}\left\langle\tau_{ij}'\frac{\partial u_i'}{\partial x_j}\right\rangle}_{E_{\mathrm{VD}}}\underbrace{+\frac{\alpha}{\rho}\left(\langle-p\delta_{ij}+\tau_{ij}\rangle\right)\left(\frac{\partial\langle u_i\rangle}{\partial x_j}-\left\langle\frac{\partial u_i}{\partial x_j}\right\rangle\right)}_{E_{\mathrm{IM}}}\\ &\underbrace{+\frac{1}{\rho V}\int_{S_I}n_j\left(-p\delta_{ij}u_i+u_i\tau_{ij}\right)\mathrm{d}S-\frac{1}{\rho V}\langle u_z\rangle\int_{S_I}n_j\left(-p\delta_{zj}+\tau_{zj}\right)\mathrm{d}S}_{E_{\mathrm{IW}}},\end{aligned}\tag{13}$$

where the left-hand side of Eq. (13) is the resulting changing rate of TKE of the fluid phase in V, terms on the right-hand side represent the rates of TKE change due to 1)"production" E_{P}, the generation of TKE due to the shear flow, 2)"turbulent transport" E_{TT}, the transport of TKE due to turbulent motion, 3)"pressure transport" E_{PT}, the transport of TKE due to pressure fluctuation, 4)"viscous transport" E_{VT}, the transport of TKE due to

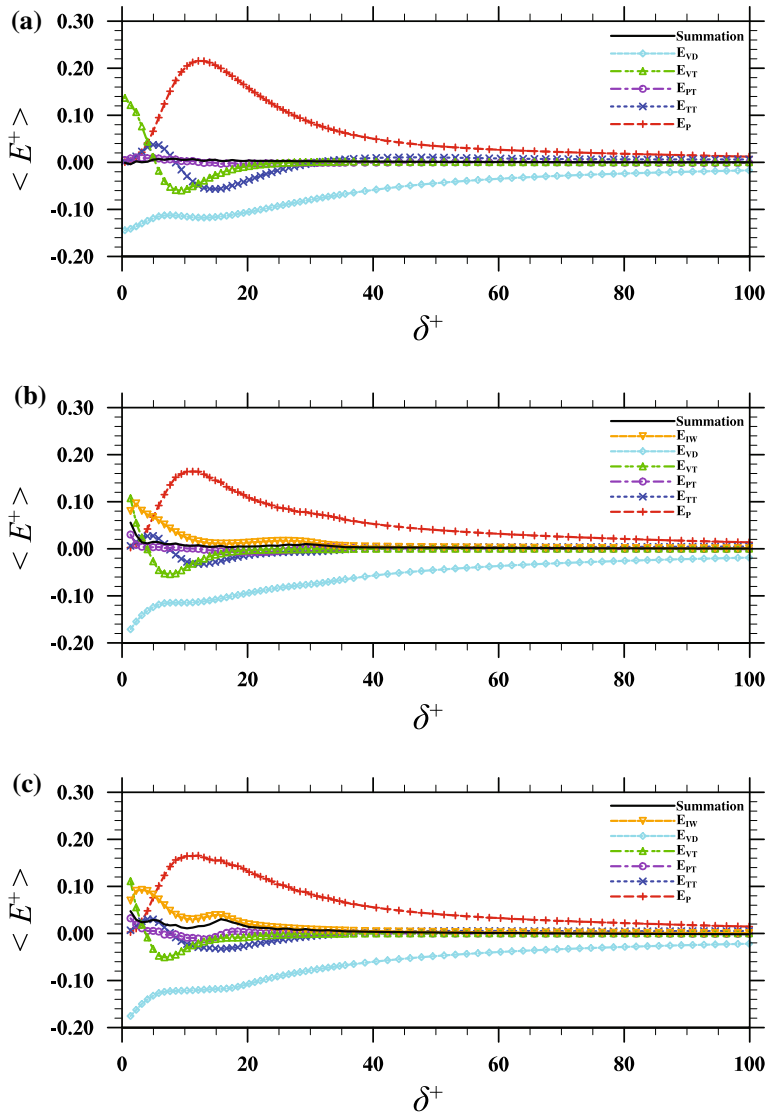

Fig. 16 Budget of TKE at the stationary state in: **a** Case p0, **b** Case p1, **c** Case p2

viscous diffusion, 5)"viscous dissipation" E_{VD}, the TKE dissipated into heat by the viscous effect, 6)"Interface moving" E_{IM}, particles moving in and out through the boundary of V, bringing in or squeezing out fluid, and 7) "Interface work" E_{IW}, the TKE generated through work done on the particle-fluid interfaces, which contains two parts, the first term in E_{IW} is the total work done by the particles and the second term in E_{IW} represents the share of this work contributes to the mechanical fluid motion. At the stationary state, when Eq. (13) is time-averaged over a sufficiently long period, the statistics of E_{IM} should become zero, since no net flux of particles should be expected in the wall-normal direction. Thus, the time-average of E_{IM} is excluded in the later discussions for simplicity.

Equation (13) is examined with the simulation data obtained in three pipe flow simulations in Fig. 16. While a perfect balance (illustrated by the black solid line in each plot) is captured in the single-phase flow simulation, in the two particle-laden flow simulations, certain derivations from the balance are noted in the near wall region $\delta^+ \leq 20$, especially in the case with small particles. These deviations are probably due to post-processing errors, i.e., the generation of turbulent statistics, which involve first- and second-order of velocity gradients calculation in cylindrical coordinates from the velocity and pressure fields on a Cartesian grid, as well as the contamination of numerical truncation errors. A similar examination of the TKE budget equation

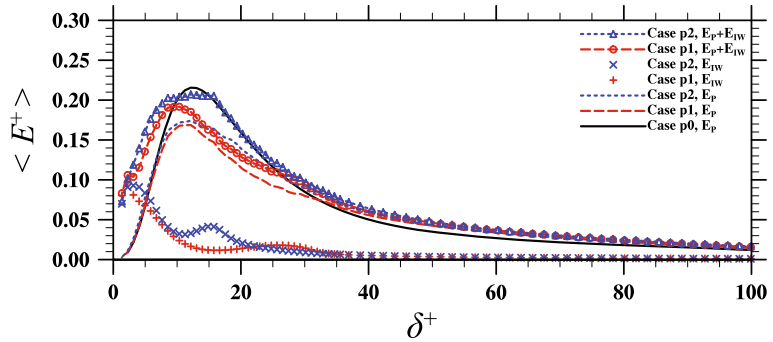

Fig. 17 The rate of TKE generation in the single-phase and particle-laden turbulent pipe flows

in the particle-laden turbulent channel flows shows much better balances [65]. Considering the existence of these errors, only a qualitative discussion of turbulence modulation based on the TKE budget equation will be provided in the later analysis.

In particle-laden turbulent pipe flows, the generation of TKE in the fluid phase is contributed not only by the production due to the mean shear E_P, but also by the particulate phase via the work done by the particle surface E_{IW}. The time-averaged profiles of E_P, E_{IW} and their combinations in each case are presented in Fig. 17. For fair comparisons, profiles in Fig. 16b, c are normalized by the local fluid volume fractions in each case, which represent the changing rate of TKE due to different mechanisms per unit fluid. As shown in Fig. 17, E_P in the particle-laden flows are significantly reduced compared to that in single-phase case. This reduction per the definition of E_P is because of the reductions in both the Reynolds stress and the mean velocity gradient in the region where E_P is significant. Since large particles result in larger reductions of both the Reynolds stress and the mean velocity gradient than small particles, E_P in the large-particle case is smaller than that in the small particle case. On the other hand, the particle work term E_{IW} is positive providing an extra production mechanism to the fluid-phase TKE, especially in the near wall region. The term E_{IW} in Eq. (13) sometimes appear in a form of $\langle u_i' f_i' \rangle$ in many previous investigations [4,12], where f_i' is the fluctuation part of the force f_i exerted on the fluid by the particles, u_i' is the fluctuation velocity of the fluid at the same location, and $\langle \cdots \rangle$ represents the ensemble averaging. However, it must be noted that while E_{IW} has a clear physical meaning, $\langle u_i' f_i' \rangle$, which is referred as the two-way coupling, depends largely on the numerical schemes used to determine how much force the fluid adjacent to a particle experiences. The combination of E_P and E_{IW} is the total rate of TKE generation in the particle-laden flows. Near the pipe wall $\delta^+ \leq 10$, the generation rate of TKE in the two particle-laden cases is significantly increased due to the extra TKE transferred from the particle phase through E_{IW}. Around the buffer region, there are regions where the addition of TKE due to E_{IW} is not sufficient to compensate the reduction of E_P. The region in the large particle case spreads to $\delta^+ = 30$ with smaller rates of TKE generation than that in the small particle case, which ends around $\delta^+ = 20$. Farther away from the wall, $\delta^+ \geq 30$, the rates of TKE generation in the particle-laden cases become larger than those in the single-phase flow due to the enhancements of E_P that attributed to the increases in mean velocity gradient in this region.

The combination of E_{TT}, E_{PT} and E_{VT} is the transport of TKE due to the inhomogeneous distribution of TKE in the radial direction, whose time-average profiles in the three pipe flow cases are presented in Fig. 18. The more homogeneous distributions of TKE observed in the particle-laden flows does not result from the fact that particles enhance the transport of TKE along the radial direction, since the rates of TKE transport are generally suppressed rather than enhanced by the presence of particles. As shown in Fig. 18, in the particle-laden cases, less TKE is transported out from the region $10 \leq \delta^+ \leq 30$ (where TKE is maximized) toward the wall (where the viscous dissipation is the strongest). This suppression of the TKE transport in the particle-laden flows are mainly due to two contributions. First, the attenuated turbulent intensity in the region $10 \leq \delta^+ \leq 30$ leads to weaker turbulent transport E_{TT} in the particle-laden cases. Second, the more homogeneous distribution of TKE results in smaller E_{VT} through the viscous diffusion. In the region $2 \leq \delta^+ \leq 10$, the magnitude of TKE transport is either enlarged or reduced by the presence of particles. However, the overall effect is to reduce the net TKE received by this region.

Finally, the viscous dissipation rates E_{VD} in the single-phase and particle-laden turbulent pipe flow simulations are shown in Fig. 19. While the dissipation rate is enhanced everywhere in the small particle case, the dissipation rate in the large-particle case is reduced in a region $10 < \delta^+ < 30$, when compared to that in the single-phase case. In a particle-laden turbulent pipe flow, the dissipation of TKE comes from two origins, the

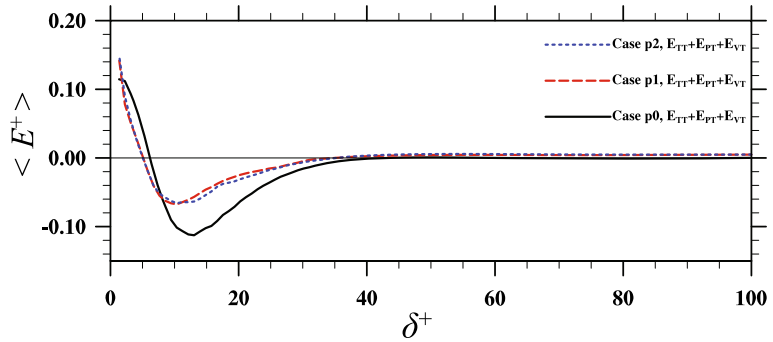

Fig. 18 The rate of TKE transport in the single-phase and particle-laden turbulent pipe flows

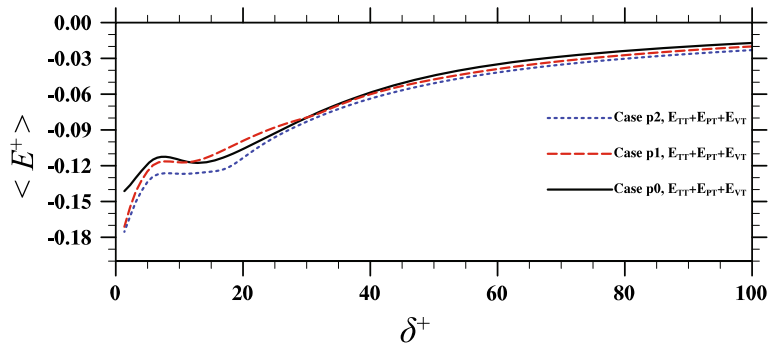

Fig. 19 The rate of TKE dissipation in the single-phase and particle-laden turbulent pipe flows

contribution from the pipe wall, and the contribution from the particle surfaces. While the presence of particles provides additional TKE dissipation on the particle surfaces, the dissipation due to the pipe wall is suppressed in the region $10 < \delta^+ < 30$ since a significantly smaller amount of TKE is produced from the shear flow when particles present. In the large-particle case, the total particle surface area is only a half of that in the small particle case, so the enhancement of dissipation rate due to the first mechanism is not sufficient to compensate the reduction triggered by the latter mechanism and a resulting reduction of dissipation rate is observed in the region $10 < \delta^+ < 30$.

The above modulations of each term in the TKE budget equation are expected to provide an qualitative explanation for the modulations of TKE observed in the particle-laden flows. Although the terms in the budget equation only represent the rates of change of TKE rather than the amount of TKE itself, we argue that a rough correspondence between the two could still be expected. The attenuation of TKE in the region $10 \leq \delta^+ \leq 30$ in the two particle-laden flows likely results from their smaller TKE generation rates in the same region. In the region $5 \leq \delta^+ \leq 10$, although the generation rates of TKE are not reduced, smaller amounts of TKE is transported into this region, so the turbulent intensity is still reduced. Closer to the wall $\delta^+ \leq 5$, the particle work supplies much higher rates of TKE generation in the particle-laden cases; thus, the turbulent intensity is augmented.

4 Summary

In this study, we conducted interface-resolved direct numerical simulations of turbulent pipe flow laden with finite-size neutrally buoyant solid particles using the lattice Boltzmann method with a sharp-interface treatment. The purposes of this study are to investigate the impact of the curvature of the pipe wall on the turbulence modulation induced by particles and clarify the mechanisms responsible for the change of turbulent intensity in such flows.

The major observations from this study are summarized below:

1. The presence of particles results in reductions of bulk flow speed in the turbulent channel and pipe flows. Large particles tend to result in larger reductions than small particles in the same flow. For a given particle size, the flow-speed reduction in the pipe flow is more significant than that in the channel flow.

2. The reductions of the bulk flow speed in the particle-laden flows are due to the smaller mean flow velocity gradients within the buffer region ($8 \leq y^+(\delta^+) \leq 30$). This is because the mean velocity gradients in the particle region, related directly to the particle angular velocities, are much smaller than that in the fluid region, which results in a globally reduced mean velocity gradients in the near wall region. Since the fluid in this region accounts for a larger portion of the total fluid volume in the pipe flow than that in the channel flow, the velocity reduction in the pipe flow is more significant. Since the large particles can impact a wider range of wall-normal locations, they can result in greater reductions of mean flow velocity than small particles.
3. Since the particles can slip along the channel or pipe wall, they tend to accelerate the flow speed very close to the walls. Although large particles have larger slip velocity than the small particles, they experience a stronger repulsive lubrication force from the wall, thus less likely to enter the near wall region; their net acceleration effect on the near wall fluid is less obvious. At a given particle size, particles in the turbulent channel flow accelerate the near wall fluid more than those in the turbulent pipe flow. This difference is partially responsible for the larger reduction of mean flow speed in the turbulent pipe flow when particles are present.
4. The mean velocity profiles of the particle-laden turbulent flows can still be fitted to a logarithmic function with modified slopes. The slopes of the logarithmic profile are larger with particles, and are not significantly dependent on the particle size. The mean velocity profiles of the present simulations are also examined against the universal logarithmic laws proposed by Luchini [68] and Costa et al. [69]. While the velocity profiles of the present simulations do converge better under those theories, more datasets are still needed to validate whether a universal log-law exists for all particle-laden wall-bounded turbulent flows. When normalized by the bulk flow speed, the mean velocity profiles in the particle-laden flows become more convex, with smaller values in the buffer region and larger values near the channel/pipe center. The mean velocity profiles in the same flow with the two particle sizes almost collapse.
5. The spatial distributions of particles in the turbulent channel and pipe flows are very similar near the walls. The profiles of particle volume fraction in both flows increase near the walls, and exhibit a local maximum close to the wall, followed by a local minimum farther away from the wall. The local maximum is due to the balance between the wall-induced repulsive force that pushing the particles away and the shear-induced lift force and the particle rotation-induced lift force both driving the particles toward the wall. The local minimum points indicate a region where the shear-induced lift force and the particle rotation-induced lift force reverse their direction. The profiles of particle volume fraction in the turbulent channel and pipe flows mainly differ in the center region. Due to the shrinking volume of the pipe flow in the center region, the particle volume fractions in the particle-laden turbulent pipe flow are larger than those in their channel flow counterparts.
6. The modulations induced by particles on the turbulent intensity are similar in the turbulent channel and pipe flows. Particles have two opposite effects on the Reynolds stress. On the one hand, particles serve as dampers to the Reynolds stress, whose effect increases with the particle size. On the other hand, particle rotation may induce additional ejection and sweeping events increasing the Reynolds stress. The latter mechanism is stronger with small particles as the small particles not only rotate faster than large particles, but also have a larger total surface area.
7. The presence of particles results in a more homogeneous distribution of turbulent kinetic energy along the wall-normal direction in both flows. TKE around the buffer region where the maximum value appears is significantly reduced by particles, while TKE in the near wall and pipe channel/pipe center regions are generally augmented. The distribution of TKE among different spatial directions is also made more isotropic by particles.
8. To understand the modulation of turbulent intensity, a budget analysis of TKE in the single-phase and particle-laden turbulent pipe flow was performed. This analysis shows that the more homogeneous distribution of TKE in particle-laden flows does not result from the fact that particles enhance the transport of TKE in the radial direction, but rather is related to the fact that the presence of particles reshapes the generation of TKE in different regions. The reduction of TKE in the region $10 \leq \delta^+ \leq 30$ is mainly attributed to the significant reduction of TKE production, while the reduction of TKE in the region $5 \leq \delta^+ \leq 10$ is mainly because less TKE is transported into this region. The augmentation of TKE in the regions $\delta^+ \leq 5$ and $\delta^+ \geq 30$ are led by the enhancements of TKE generation due to the inter-phase transfer and production, respectively.

The above observations should be taken as preliminary results since the lubrication force model and the soft-sphere collision model used to handle the particle–wall interaction may affect the slip velocity of particles

near the pipe wall. Furthermore, in the present work, the tangential lubrication force correction is not included and the soft-sphere collision ignores the effect of particle rotation. A systematic investigation on the effects of the lubrication force model and collision models will be considered in the future to further support the observations in this study.

Acknowledgements This work has been supported by the U.S. National Science Foundation (NSF) under grants CNS1513031 and CBET-1706130, and by the Southern University of Science and Technology, China. Computing resources are provided by National Center for Atmospheric Research through CISL-P35751014, and CISL-UDEL0001.

References

1. Balachandar, S., Eaton, J.K.: Turbulent dispersed multiphase flow. Annu. Rev. Fluid Mech. **42**, 111 (2010)
2. Gore, R.A., Crowe, C.T.: Effect of particle size on modulating turbulent intensity. Int. J. Multiph. Flow **15**(2), 279 (1989)
3. Gore, R.A., Crowe, C.T.: Modulation of turbulence by a dispersed phase. J. Fluids Eng. **113**(2), 304 (1991)
4. Kulick, J.D., Fessler, J.R., Eaton, J.K.: Particle response and turbulence modification in fully developed channel flow. J. Fluid Mech. **277**, 109 (1994)
5. Paris, A.D.: Turbulence attenuation in a particle-laden channel flow. Ph.d. dissertation, Stanford University (2001)
6. Kussin, J., Sommerfeld, M.: Experimental studies on particle behaviour and turbulence modification in horizontal channel flow with different wall roughness. Exp. Fluids **33**(1), 143 (2002)
7. Tanaka, T., Eaton, J.K.: Classification of turbulence modification by dispersed spheres using a novel dimensionless number. Phys. Rev. Lett. **101**(11), 114502 (2008)
8. Bellani, G., Byron, M.L., Collignon, A.G., Meyer, C.R., Variano, E.A.: Shape effects on turbulent modulation by large nearly neutrally buoyant particles. J. Fluid Mech. **712**, 41 (2012)
9. Eaton, J.K.: Two-way coupled turbulence simulations of gas-particle flows using point-particle tracking. Int. J. Multiph. Flow **35**(9), 792 (2009)
10. Tanaka, T., Eaton, J.K.: Sub-Kolmogorov resolution partical image velocimetry measurements of particle-laden forced turbulence. J. Fluid Mech. **643**, 177 (2010)
11. Prosperetti, A.: Life and death by boundary conditions. J. Fluid Mech. **768**, 1 (2015)
12. Lucci, F., Ferrante, A., Elghobashi, S.: Modulation of isotropic turbulence by particles of Taylor length-scale size. J. Fluid Mech. **650**, 5 (2010)
13. Gao, H., Li, H., Wang, L.P.: Lattice Boltzmann simulation of turbulent flow laden with finite-size particles. Comput. Math. Appl. **65**(2), 194 (2013)
14. Ten Cate, A., Derksen, J.J., Portela, L.M., Van Den Akker, H.E.: Fully resolved simulations of colliding monodisperse spheres in forced isotropic turbulence. J. Fluid Mech. **519**, 233 (2004)
15. Vreman, A.W.: Particle-resolved direct numerical simulation of homogeneous isotropic turbulence modified by small fixed spheres. J. Fluid Mech. **796**, 40 (2016)
16. Shao, X., Wu, T., Yu, Z.: Fully resolved numerical simulation of particle-laden turbulent flow in a horizontal channel at a low Reynolds number. J. Fluid Mech. **693**, 319 (2012)
17. Picano, F., Breugem, W.P., Brandt, L.: Turbulent channel flow of dense suspensions of neutrally buoyant spheres. J. Fluid Mech. **764**, 463 (2015)
18. Maxey, M.: Simulation methods for particulate flows and concentrated suspensions. Annu. Rev. Fluid Mech. **49**, 171 (2017)
19. Hu, H.H., Patankar, N.A., Zhu, M.: Direct numerical simulations of fluid-solid systems using the arbitrary Lagrangian–Eulerian technique. J. Comput. Phys. **169**(2), 427 (2001)
20. Burton, T.M., Eaton, J.K.: Fully resolved simulations of particle–turbulence interaction. J. Fluid Mech. **545**, 67 (2005)
21. Zeng, L., Balachandar, S., Fischer, P., Najjar, F.: Interactions of a stationary finite-sized particle with wall turbulence. J. Fluid Mech. **594**, 271 (2008)
22. Zhang, Z., Prosperetti, A.: A second-order method for three-dimensional particle simulation. J. Comput. Phys. **210**(1), 292 (2005)
23. Sierakowski, A.J., Prosperetti, A.: Resolved-particle simulation by the Physalis method: enhancements and new capabilities. J. Comput. Phys. **309**, 164 (2016)
24. Botto, L., Prosperetti, A.: A fully resolved numerical simulation of turbulent flow past one or several spherical particles. Phys. Fluids **24**(1), 013303 (2012)
25. Uhlmann, M.: Interface-resolved direct numerical simulation of vertical particulate channel flow in the turbulent regime. Phys. Fluids **20**(5), 053305 (2008)
26. Uhlmann, M.: An immersed boundary method with direct forcing for the simulation of particulate flows. J. Comput. Phys. **209**(2), 448 (2005)
27. Breugem, W.P.: A second-order accurate immersed boundary method for fully resolved simulations of particle-laden flows. J. Comput. Phys. **231**(13), 4469 (2012)
28. Glowinski, R., Pan, T.W., Hesla, T.I., Joseph, D.D.: A distributed Lagrange multiplier/fictitious domain method for particulate flows. Int. J. Multiph. Flow **25**(5), 755 (1999)
29. Yu, Z., Shao, X.: A direct-forcing fictitious domain method for particulate flows. J. Comput. Phys. **227**(1), 292 (2007)
30. Wu, T.H., Shao, X.M., Yu, Z.S.: Fully resolved numerical simulation of turbulent pipe flows laden with large neutrally-buoyant particles. J. Hydrodyn. Ser. B **23**(1), 21 (2011)
31. Wang, L.P., Ayala, O., Gao, H., Andersen, C., Mathews, K.L.: Study of forced turbulence and its modulation by finite-size solid particles using the lattice Boltzmann approach. Comput. Math. Appl. **67**(2), 363 (2014)

32. Wang, L.P., Peng, C., Guo, Z., Yu, Z.: Lattice Boltzmann simulation of particle-laden turbulent channel flow. Comput. Fluids **124**, 226 (2016)
33. Eshghinejadfard, A., Abdelsamie, A., Hosseini, S.A., Thévenin, D.: Immersed boundary lattice Boltzmann simulation of turbulent channel flows in the presence of spherical particles. Int. J. Multiph. Flow **96**, 161 (2017)
34. Chen, S., Doolen, G.D.: Lattice Boltzmann method for fluid flows. Annu. Rev. Fluid Mech. **30**(1), 329 (1998)
35. Aidun, C.K., Clausen, J.R.: Lattice-Boltzmann method for complex flows. Annu. Rev. Fluid Mech. **42**, 439 (2010)
36. Ladd, A.J.C.: Numerical simulations of particulate suspensions via a discretized Boltzmann equation. Part 1. Theoretical foundation. J. Fluid Mech. **271**(1), 285 (1994)
37. Aidun, C.K., Lu, Y., Ding, E.J.: Direct analysis of particulate suspensions with inertia using the discrete Boltzmann equation. J. Fluid Mech. **373**, 287 (1998)
38. Huffman, G.D., Bradshaw, P.: A note on von Karman's constant in low Reynolds number turbulent flows. J. Fluid Mech. **53**, 45 (1972)
39. Loulou, P., Moser, R.D., Mansour, N.N.: Direct numerical simulation of incompressible pipe flow using a B-spline spectral method. NASA Tech. Memo. No. **110436**, 1997 (1997)
40. Wu, X., Moin, P.: A direct numerical simulation study on the mean velocity characteristics in turbulent pipe flow. J. Fluid Mech. **608**, 81 (2008)
41. Kim, J., Moin, P., Moser, R.: Turbulence statistics in fully developed channel flow at low Reynolds number. J. Fluid Mech. **177**, 133 (1987)
42. Pope, S.B.: Turbulent Flows. IOP Publishing, Bristol (2001)
43. Chin, C., Ooi, A.S.H., Marusic, I.: The influence of pipe length on turbulence statistics computed from direct numerical simulation data. Phys. Fluids **22**, 115107 (2010)
44. Xu, Y., Subramaniam, S.: Effect of particle clusters on carrier flow turbulence: a direct numerical simulation study. Flow Turbul. Combust. **85**(3), 735 (2010)
45. White, A.T., Chong, C.K.: Rotational invariance in the three-dimensional lattice Boltzmann method is dependent on the choice of lattice. J. Comput. Phys. **230**, 6367 (2011)
46. Kang, S.K., Hassan, Y.A.: The effect of lattice models within the lattice Boltzmann method in the simulation of wall-bounded turbulent flows. J. Comput. Phys. **232**, 100 (2013)
47. Peng, C., Geneva, N., Guo, Z., Wang, L.P.: Direct numerical simulation of turbulent pipe flow using the lattice Boltzmann method. J. Comput. Phys. **357**, 16 (2018)
48. d'Humières, D., Ginzburg, I., Krafczyk, M.: Multiple-relaxation-time lattice Boltzmann models in three-dimensions. Philos. Trans. R. Soc. A **360**, 437 (2002)
49. Suga, K., Kuwata, Y., Takashima, K.: A D3Q27 multiple-relaxation-time lattice Boltzmann method for turbulent flows. Comput. Math. Appl. **69**, 518 (2015)
50. Junk, M., Klar, A., Luo, L.S.: Asymptotic analysis of the lattice Boltzmann equation. J. Comput. Phys. **210**, 676 (2005)
51. Dellar, P.J.: Bulk and shear viscosities in lattice Boltzmann equations. Phys. Rev. E **64**(3), 031203 (2001)
52. Feng, Z.G., Michaelides, E.E.: Proteus: a direct forcing method in the simulations of particulate flows. J. Comput. Phys. **202**(1), 20 (2005)
53. Kang, S.K., Hassan, Y.A.: A comparative study of direct-forcing immersed boundary-lattice Boltzmann methods for stationary complex boundaries. Int. J. Numer. Methods Fluids **66**(9), 1132 (2011)
54. Bouzidi, M., Firdaouss, M., Lallemand, P.: Momentum transfer of a Boltzmann-lattice fluid with boundaries. Phys. Fluids **13**(11), 3452 (2001)
55. Yu, D., Mei, R., Luo, L.S., Shyy, W.: Viscous flow computations with the method of lattice Boltzmann equation. Prog. Aerosp. Sci. **39**(5), 329 (2003)
56. Zhao, W., Yong, W.A.: Single-node second-order boundary schemes for the lattice Boltzmann method. J. Comput. Phys. **329**(6), 1 (2017)
57. Peng, Y., Luo, L.S.: A comparative study of immersed-boundary and interpolated bounce-back methods in LBE. Prog. Comput. Fluid Dyn. Int. J. **8**(1–4), 156 (2008)
58. Chen, L., Yu, Y., Lu, J., Hou, G.: A comparative study of lattice Boltzmann methods using bounce-back schemes and immersed boundary ones for flow acoustic problems. Int. J. Numer. Methods Fluids **74**(6), 439 (2014)
59. Mei, R., Yu, D., Shyy, W., Luo, L.S.: Force evaluation in the lattice Boltzmann method involving curved geometry. Phys. Rev. E **65**(4), 041203 (2002)
60. Wen, B., Zhang, C., Tu, Y., Wang, C., Fang, H.: Galilean invariant fluid-solid interfacial dynamics in lattice Boltzmann simulations. J. Comput. Phys. **266**, 161 (2014)
61. Peng, C., Teng, Y., Hwang, B., Guo, Z., Wang, L.P.: Implementation issues and benchmarking of lattice Boltzmann method for moving rigid particle simulations in a viscous flow. Comput. Math. Appl. **72**(2), 349 (2016)
62. Tao, S., Hu, J., Guo, Z.: An investigation on momentum exchange methods and refilling algorithms for lattice Boltzmann simulation of particulate flows. Comput. Fluids **133**, 1 (2016)
63. Caiazzo, A.: Analysis of lattice Boltzmann nodes initialisation in moving boundary problems. Prog. Comput. Fluid Dyn. Int. J. **8**(1–4), 3 (2008)
64. Brändle de Motta, J.C., Breugem, W.P., Gazanion, B., Estivalezes, J.L., Vincent, S., Climent, E.: Numerical modelling of finite-size particle collisions in a viscous fluid. Phys. Fluids **25**(8), 083302 (2013)
65. Peng, C.: Study of turbulence modulation by finite-size solid particles with the lattice Boltzmann method. Ph.D. dissertation, the University of Delaware (2018)
66. El Khoury, G.K., Schlatter, P., Noorani, A., Fischer, P.F., Brethouwer, G., Johansson, A.V.: Direct numerical simulation of turbulent pipe flow at moderately high Reynolds numbers. Flow Turbul. Combust. **91**(3), 475 (2013)
67. Wagner, C., Huttl, T.J., Friedrich, R.: Low-Reynolds-number effects derived from direct numerical simulations of turbulent pipe flow. Comput. Fluids **30**, 581 (2001)
68. Luchini, P.: Universality of the turbulent velocity profile. Phys. Rev. Lett. **118**(22), 224501 (2017)

69. Costa, P., Picano, F., Brandt, L., Breugem, W.P.: Universal scaling laws for dense particle suspensions in turbulent wall-bounded flows. Phys. Rev. Lett. **117**(13), 134501 (2016)
70. Hall, D.: Measurements of the mean force on a particle near a boundary in turbulent flow. J. Fluid Mech. **187**, 451 (1988)
71. Saffman, P.: The lift on a small sphere in a slow shear flow. J. Fluid Mech. **22**(2), 385 (1965)
72. Segré, G., Silberberg, A.: Behaviour of macroscopic rigid spheres in Poiseuille flow Part 2. Experimental results and interpretation. J. Fluid Mech. **14**(1), 136 (1962)
73. Crowe, C.T., Schwarzkopf, J.D., Sommerfeld, M., Tsuji, Y.: Multiphase Flows with Droplets and Particles. CRC Press, Boca Raton (2011)